

A Bayesian estimation method for variational phase-field fracture problems

Amirreza Khodadadian^{a,c,*}, Nima Noii^c, Maryam Parvizi^a, Mostafa Abbaszadeh^b, Thomas Wick^c, Clemens Heitzinger^{a,d}

^a*Institute of Analysis and Scientific Computing, Vienna University of Technology (TU Wien), Wiedner Hauptstraße 8–10, 1040 Vienna, Austria*

^b*Faculty of Mathematics and Computer Sciences, Amirkabir University of Technology, No. 424, Hafez Ave., 15914, Tehran, Iran*

^c*Institute of Applied Mathematics, Leibniz University Hannover, Welfengarten 1, 30167 Hanover, Germany*

^d*School of Mathematical and Statistical Sciences, Arizona State University, Tempe, AZ 85287, USA*

Abstract

In this work, we propose a parameter estimation framework for fracture propagation problems. The fracture problem is described by a phase-field method. Parameter estimation is realized with a Bayesian framework. Here, the focus is on uncertainties arising in the solid material parameters and the critical energy release rate. A reference value (obtained on a sufficiently small mesh) as the replacement of measurement will be chosen, and their posterior distribution is obtained. Due to time- and mesh dependency of the problem, the computational costs can be high. Using Bayesian inversion, we solve the problem on a relatively coarse mesh and fit the parameters. The obtained load-displacement curve that is usually the target function is matched with the reference values. Finally, our algorithmic approach is substantiated with several numerical examples.

Keywords: Bayesian estimation, inverse problem, phase-field propagation, brittle fracture, multi-field problem.

1. Introduction

This work is devoted to the quantification of uncertainties in fracture failure problems. To formulate fracture phenomena, the phase-field formulation for the quasi-brittle fracture solid is used. The variational phase-field formulation is a thermodynamically consistent framework to compute the fracture failure process. This formulation emanates from the regularized version of the sharp crack surface function [1]. The regularized fracture phenomena are described with an additional auxiliary smooth indicator function, which is denoted as crack phase-field. Along, with a mechanical field (denoted by \mathbf{u}), a minimization problem for the multi-field problem (\mathbf{u}, d) can be formulated. The main feature of variational formulation arises from the crack phase-field is to approximate the discontinuities in the \mathbf{u} across the lower-dimensional crack topology with the d [2].

The resulting, regularized formulation leads to a diffusive transition zone between two phases in the solid, which corresponds to the fractured phase (i.e., $d = 0$) and intact phase (i.e., $d = 1$), respectively. The transition zone which

*Corresponding author

Email addresses: khodadadian@ifam.uni-hannover.de (Amirreza Khodadadian), noii@ifam.uni-hannover.de (Nima Noii), maryam.parvizi@tuwien.ac.at (Maryam Parvizi), m.abbaszadeh@aut.ac.ir (Mostafa Abbaszadeh), thomas.wick@ifam.uni-hannover.de (Thomas Wick), clemens.heitinger@tuwien.ac.at (Clemens Heitzinger)

is affected by a regularized parameter known as length-scale (denoted by l). Moreover, the regularized parameter l is related to the element size h . Specifically, $h := l(h)$ hold such that $h \ll l$ through discretization error estimates [3, 4]. Therefore, sufficiently small regularized length-scale is computationally demanding. To date, the focus in such cases was on local mesh adaptivity and parallel computing in order to reduce the computational cost significantly; see for instance [5, 6, 7, 8, 9, 10, 11, 12, 13]. Another recent approach is a global-local technique in which parts of the domain are solved with a simplified approach [14, 15] that also aims to reduce the computational cost.

The main goal in this work is to quantify uncertain parameters of the phase-field formulation. The underlying framework of parameter estimation using Bayesian inference is described in the following. Bayesian inference is a probabilistic method used to estimate the unknown parameters according to the prior knowledge. The observations (experimental or synthetic measurements) can be used to update the prior data and provide the posterior estimation. The distribution provides useful information about the possible range of parameters and their variations and mean. Markov chain Monte Carlo (MCMC) [16] is a common computational approach for extracting information of the inverse problem (posterior distribution). Metropolis-Hastings (MH) algorithm [17] is the most popular MCMC method to generate a Markov chain employing a proposal distribution for new steps. In practice, a reliable estimation of influential parameters is not possible or needs significant efforts. In [18, 19], the authors used the Metropolis-Hastings algorithm to estimate the unknown parameters in field-effect sensors. It enables authors to estimate **PT**-density of the target molecules which can not be experimentally estimated. The interested reader refers to [20, 21] for more application of Bayesian estimation in applied science. In the same line, other optimization approach can be used to determine intrinsic material properties of the specimen from experimental load-displacement curve, see e.g., [22].

The current work follows two goals. First, using Bayesian inversion to determine the unknown and effective phase-field fracture parameters, i.e., Lamé 1st parameter and shear modulus as well as Griffith’s critical elastic energy release rate. To this end, a reference value (obtained on a sufficiently refined mesh) as the replacement of measurement will be chosen, and their posterior distribution is obtained. The second goal is related to the temporal and spatial mesh dependencies of the problem. The computational costs can be high, specifically when an appropriate estimation is required. Specifically, when we aim to have a variational phase-field modeling within multi-physics framework, see e.g. [23, 24, 25]. Using Bayesian inversion; we strive to solve the problem with a coarser mesh and fit the parameters. The obtained load-displacement curve (as an important characteristic) is matched with the reference value. In spite of using coarser meshes and therefore significantly lower computational costs (in terms of CPU timings), the accuracy of the solution is reliable (crack initiation and material fracture time estimated precisely).

The paper is organized as follows: In Section 2, we describe the variational isotropic phase-field formulation for the brittle fracture that is a thermodynamically consistent framework to compute the fracture failure process. In section 3, the Bayesian inference is explained. We describe how the MH algorithm will be used to estimate the unknown parameters in phase-field fracture. Also we point out the critical points in the load-displacement curve, which must be estimated precisely with the Bayesian approach. In Section 4, the Bayesian framework is adopted to estimate unknown parameters in the phase-field fracture approach. In Section 5, three specific numerical examples

with different parameters and geometry will be given. We will use two proposal distributions (uniform and normal distribution) to sample the candidates and estimate the unknown parameters with different mesh sizes. Finally, in 6 we will draw paper conclusions and explain our future planes for employing Bayesian inversion in heterogeneous materials.

2. Variational isotropic phase-field brittle fracture

2.1. The primary fields for the variational phase-field formulation

We consider a smooth, open and bounded domain $\Omega \subset \mathbb{R}^\delta$, $\delta \in \{2, 3\}$. In this computational domain, a lower dimensional fracture can be indicated by $C \subset \mathbb{R}^{\delta-1}$. In the following, Dirichlet boundaries conditions indicated as $\partial\Omega_D := \partial\Omega$, and Neumann boundaries conditions are given on $\partial_N\Omega := \Gamma_N \cup \partial C$, where Γ_N is the outer boundary of Ω and ∂C is the crack boundary. The geometric setup including notations is illustrated in Figure 1a. The surface fracture C is estimated in $\Omega_F \subset \Omega \subset \mathbb{R}^\delta$. A region without any fracture (i.e., an intact region) is indicated by $\Omega_R := \Omega \setminus \Omega_F \subset \Omega \subset \mathbb{R}^\delta$ such that $\Omega_R \cup \Omega_F = \Omega$ and $\Omega_R \cap \Omega_F = \emptyset$.

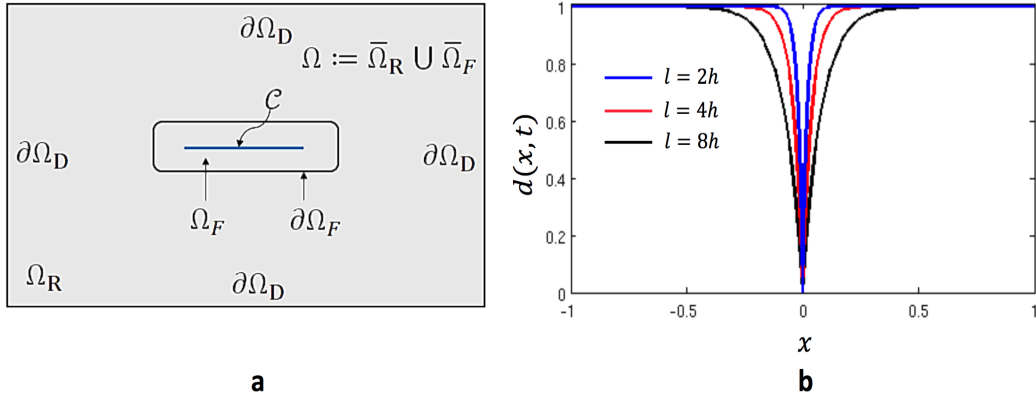


Figure 1: (a) Geometric setup: the intact region indicated by Ω_R and C is the crack phase-field surface. The entire domain is denoted by Ω . The crack phase-field is approximated in the domain Ω_F . The fracture boundary is $\partial\Omega_F$ and the outer boundary of the domain is $\partial\Omega$. Ω_F is represented by means of d such that the transition area is $0 < d < 1$ with thickness $2l$. (b) Regularized crack phase-field profile for a different length scale. A smaller value for the length scale lets the crack phase-field profile converge to a delta distribution.

The variational phase-field formulation is a thermodynamically consistent framework to compute the fracture process. Due to the presence of the crack surface, we formulate the fracture problem as a two-field problem including the displacement field $\mathbf{u}(\mathbf{x}): \Omega \rightarrow \mathbb{R}^\delta$ and the crack phase-field $d(\mathbf{x}): \Omega \rightarrow [0, 1]$. The crack phase-field function $d(\mathbf{x})$ interpolates between $d = 1$, which indicates undamaged material, and $d = 0$, which indicates a fully broken material phase.

For stating the variational formulations, the spaces

$$\begin{aligned} V &:= \{\mathbf{H}^1(\Omega)^\delta : \mathbf{u} = \bar{\mathbf{u}} \text{ on } \partial\Omega_D\}, \\ W &:= \mathbf{H}^1(\Omega), \\ W_{in} &:= \{d \in \mathbf{H}^1(\Omega)^{\delta-1} : 0 \leq d \leq d^{old}\} \end{aligned} \quad (1)$$

are used. Herein, W_{in} denotes a closed, non-empty and convex set which is a subset of the linear function space $W = \mathbf{H}^1(\Omega)$ (see e.g., [26]).

2.2. Variational formulation for the mechanical contribution

In the following, a variational setting for quasi-brittle fracture in bulk materials with small deformations is formulated. To formulate the bulk free energy stored in the material, we define the first and second invariants as

$$I_1(\boldsymbol{\varepsilon}) = \text{tr}(\boldsymbol{\varepsilon}), \quad I_2(\boldsymbol{\varepsilon}) = \text{tr}(\boldsymbol{\varepsilon}^2), \quad (2)$$

with the second-order infinitesimal small strain tensor defined as

$$\boldsymbol{\varepsilon} = \nabla_s \mathbf{u} = \text{sym}[\nabla \mathbf{u}]. \quad (3)$$

The isotropic scalar valued free-energy function reads

$$\widetilde{\Psi}(I_1(\boldsymbol{\varepsilon}), I_2(\boldsymbol{\varepsilon})) := \frac{\lambda}{2} I_1^2 + \mu I_2, \quad (4)$$

with the elastic Lamé constants denoted by $\lambda > 0$ and $\mu > 0$. A stress-free condition for the bulk energy-density function requires $\widetilde{\Psi}(I_1(\mathbf{0}), I_2(\mathbf{0})) = 0$. Hence, the bulk free-energy functional including the stored internal energy and the imposed external energy is

$$\mathcal{E}_{bulk}(\mathbf{u}) = \int_{\Omega_C} \widetilde{\Psi}(\boldsymbol{\varepsilon}) d\mathbf{x} - \int_{\partial_N \Omega_C} \boldsymbol{\tau} \cdot \mathbf{u} d\mathbf{s} \quad (5)$$

where $\boldsymbol{\tau}$ is the imposed traction vector on $\partial_N \Omega_C := \Gamma_N \cup C$.

Following [1], we define the total energetic functional which includes the stored bulk-energy functional and fracture dissipation as

$$\mathcal{E}(\mathbf{u}, C) = \mathcal{E}_{bulk}(\mathbf{u}) + G_c \mathcal{H}^{\delta-1}(C), \quad (6)$$

where G_c is the so called the Griffith's critical elastic-energy release rate. Also, $\mathcal{H}^{\delta-1}$ refers to the $(\delta - 1)$ -dimensional Hausdorff measure (see e.g. [2]). Following [2], $\mathcal{H}^{\delta-1}$ is regularized (i.e. approximated) by the crack phase-field $d(\mathbf{x})$ (see e.g. [2]). Doing so, a second-order variational phase-field formulation is employed; see Section 2.3. Additionally to that, a second-order stress degradation state function (*intact-to-fractured transition* formulation) is used as a monotonically decreasing function which is lower semi-continuous order; see Section 2.5.

2.3. Crack phase-field formulation in a regularized setting

Let us represent a regularized (i.e., approximated) crack surface for the sharp-crack topology (which is a Kronecker delta function) through the exponential function $d(\mathbf{x}) = 1 - \exp^{-|\mathbf{x}|/l}$, which satisfies $d(\mathbf{x}) = 0$ at $\mathbf{x} = 0$ as a Dirichlet boundary condition and $d(\mathbf{x}) = 1$ as $\mathbf{x} \rightarrow \pm\infty$. This is explicitly shown in Figure 1b for different length scales. A regularized crack surface energy functional is

$$G_c \mathcal{H}^{\delta-1}(C) := G_c \int_{\Omega} \gamma_l(d, \nabla d) \, d\mathbf{x} \quad \text{with} \quad \gamma_l(d, \nabla d) := \frac{1}{2l}(1-d)^2 + \frac{l}{2} \nabla d \cdot \nabla d \quad (7)$$

based on the crack surface density function γ_l per unit volume of the solid. The equation is so-called AT2 model because of the quadratic term in PDE.

We set sharp crack surfaces as Dirichlet boundary conditions in $C \subset \Omega$. Hence, the crack phase-field $d(x, t)$ is obtained from the minimization of the regularized crack density function as

$$d(\mathbf{x}) = \underset{d(\mathbf{x}) \in W_{in} \text{ with } d(\mathbf{x})=0 \, \forall \mathbf{x} \in C}{\operatorname{argmin}} \int_{\Omega} \gamma_l(d, \nabla d) \, d\mathbf{x}. \quad (8)$$

Figure 2 gives the numerical solution that arises from the minimization Eq. 8 and demonstrates the effect of different regularized length scales on the numerical solution. Clearly, a smaller length scale leads to a narrower transition zone (see Figure 2c). That is also in agreement with the crack phase-field profile shown in Figure 1b.

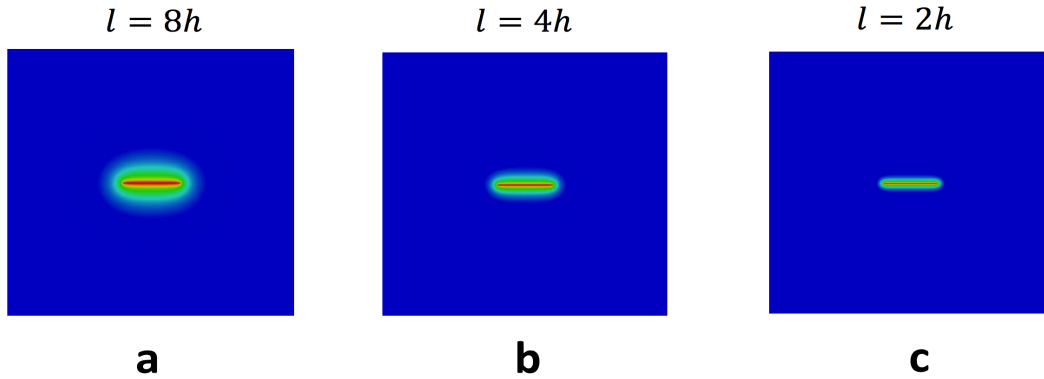


Figure 2: Effect of different length scales on the crack phase-field resolution as calculated by the minimization problem in Eq. 8 such that $l_a > l_b > l_c$.

2.4. Strain-energy decomposition for the bulk free-energy

Fracture mechanics is the process which results in the compression free state. As a result, a fracture process behaves differently in the *tension phase* and in *compression phase*, see e.g. [27]. In the following, an additive split for the strain energy density function to distinguish the tension and compression phases is used. Instead of dealing with a full linearized strain tensor $\boldsymbol{\varepsilon}(\mathbf{u})$, the additive decomposition

$$\boldsymbol{\varepsilon}(\mathbf{u}) = \boldsymbol{\varepsilon}^+(\mathbf{u}) + \boldsymbol{\varepsilon}^-(\mathbf{u}) \quad \text{with} \quad \boldsymbol{\varepsilon}^\pm(\mathbf{u}) := \sum_{i=1}^{\delta} \langle \varepsilon_i \rangle^\pm \mathbf{N}_i \otimes \mathbf{N}_i$$

of the strain tensor based on its eigenvalues is used [28, 7]. Herein, $\langle x \rangle_{\pm} := \frac{x \pm |x|}{2}$ refers to the a Macaulay brackets for $x \in \mathbb{R}^{\pm}$. Furthermore, $\boldsymbol{\varepsilon}^+$ and $\boldsymbol{\varepsilon}^-$ refer to the tension and compression parts of the strain, respectively. The $\{\varepsilon_i\}$ are the principal strains (i.e., the eigenvalues of the $\boldsymbol{\varepsilon}(\mathbf{u})$) and the $\{\mathbf{N}_i\}$ are the principal strain directions (i.e., the eigenvectors of the $\boldsymbol{\varepsilon}(\mathbf{u})$). To determine the tension and compression parts of total strain $\boldsymbol{\varepsilon}$, a positive-negative fourth-order projection tensor is

$$\mathbb{P}_{\boldsymbol{\varepsilon}}^{\pm} := \frac{\partial \boldsymbol{\varepsilon}^{\pm}}{\partial \boldsymbol{\varepsilon}} = \frac{\partial (\sum_{i=1}^{\delta} \langle \varepsilon_i \rangle^{\pm} \mathbf{N}_i \otimes \mathbf{N}_i)}{\partial \boldsymbol{\varepsilon}} \quad (9)$$

such that the fourth-order projection tensor $\mathbb{P}_{\boldsymbol{\varepsilon}}^{\pm}$ projects the total linearized strain $\boldsymbol{\varepsilon}$ onto its tension-compression counterparts, i.e., $\boldsymbol{\varepsilon}^{\pm} = \mathbb{P}_{\boldsymbol{\varepsilon}}^{\pm} : \boldsymbol{\varepsilon}$. Hence an additive formulation of the strain-energy density function consisting of the tension and the compression parts reads

$$\Psi(I_1(\boldsymbol{\varepsilon}), I_2(\boldsymbol{\varepsilon})) := \underbrace{\widetilde{\Psi}^+(I_1^+(\boldsymbol{\varepsilon}), I_2^+(\boldsymbol{\varepsilon}))}_{\text{tension term}} + \underbrace{\widetilde{\Psi}^-(I_1^-(\boldsymbol{\varepsilon}), I_2^-(\boldsymbol{\varepsilon}))}_{\text{compression term}}. \quad (10)$$

Here, the scalar valued principal invariants in the positive and negative modes are

$$I_1^{\pm}(\boldsymbol{\varepsilon}) := \langle I_1(\boldsymbol{\varepsilon}) \rangle_{\pm}, \quad I_2^{\pm}(\boldsymbol{\varepsilon}) := I_2(\boldsymbol{\varepsilon}^{\pm}). \quad (11)$$

2.5. Energy functional for the isotropic crack topology

Due to the physical response of the fracture process, it is assumed that the degradation of the bulk material due to the crack propagation depends only on the tensile and isochoric counterpart of the stored bulk energy density function. Thus, there is no degradation of the bulk material in compression mode, see [28]. Hence, the degradation function denoted as $g(d_+)$ acts only on the positive part of bulk energy given in Eq. 10, i.e.,

$$g(d_+) := d_+^2, \quad g: [0, 1] \rightarrow [0, 1]. \quad (12)$$

This function results in degradation of the solid during the evolving crack phase-field parameter d . Due to the transition between the intact region and the fractured phase, the degradation function has flowing properties, i.e.,

$$g(0) = 0, \quad g(1) = 1, \quad g(c) > 0 \text{ for } c > 0, \quad g'(0) = 0, \quad g'(1) > 0. \quad (13)$$

Following [28], the small residual scalar $0 < \kappa \ll 1$ is introduced to prevent numerical instabilities. It is imposed on the degradation function, which now reads

$$g(d_+) := (1 - \kappa)d_+^2 + \kappa, \quad g: [0, 1] \rightarrow [0, 1]. \quad (14)$$

The stored bulk density function is denoted as w_{bulk} . Together with the fracture density function w_{frac} , it gives the the total density function

$$w(\boldsymbol{\varepsilon}, d, \nabla d) = w_{bulk}(\boldsymbol{\varepsilon}, d) + w_{frac}(d, \nabla d) \quad (15)$$

with

$$w_{bulk}(\boldsymbol{\varepsilon}, d) = g(d_+) \widetilde{\Psi}^+(I_1^+(\boldsymbol{\varepsilon}), I_2^+(\boldsymbol{\varepsilon})) + \widetilde{\Psi}^-(I_1^-(\boldsymbol{\varepsilon}), I_2^-(\boldsymbol{\varepsilon})), \quad (16)$$

$$w_{frac}(d, \nabla d) = G_c \gamma_I(d, \nabla d).$$

Formulation 2.1 (Energy functional for isotropic crack topology). *We assume that λ and μ are given as well as initial conditions $\mathbf{u}_0 = \mathbf{u}(\mathbf{x}, 0)$ and $d_0 = d(\mathbf{x}, 0)$. For the loading increments $n \in \{1, 2, \dots, N\}$, find $\mathbf{u} := \mathbf{u}^n \in V$ and $d := d^n \in W_{in}$ such that the functional*

$$\begin{aligned} \mathcal{E}(\mathbf{u}, d) &= \mathcal{E}_{bulk}(\mathbf{u}, d_+, \chi) + \mathcal{E}_{frac}(d) + \mathcal{E}_{ext}(\mathbf{u}) \\ &= \underbrace{\int_{\Omega} g(d_+) \tilde{\Psi}^+(I_1^+, I_2^+) + \tilde{\Psi}^-(I_1^-, I_2^-) \, d\mathbf{x}}_{\text{bulk term}} + \underbrace{G_c \int_{\Omega} \gamma_l(d, \nabla d) \, d\mathbf{x}}_{\text{fracture term}} - \underbrace{\int_{\partial_N \Omega} \bar{\boldsymbol{\tau}} \cdot \mathbf{u} \, ds}_{\text{external load}}, \end{aligned}$$

is minimized.

Herein, to make sure that phase-field quantity d lies in the interval $[0, 1]$, we define d_+ to map negative values of d to positive values. In Formulation 2.1, the stationary points of the energy functional are determined by the first-order necessary conditions, namely the Euler-Lagrange equations, which can be found by differentiation with respect to \mathbf{u} and d .

Formulation 2.2 (Euler-Lagrange equations). *Let λ, μ be given as well as the initial conditions $\mathbf{u}_0 = \mathbf{u}(\mathbf{x}, 0)$ and $d_0 = d(\mathbf{x}, 0)$. For the loading increments $n \in \{1, 2, \dots, N\}$, find $\mathbf{u} := \mathbf{u}^n \in V$ and $d := d^n \in W_{in}$ such that*

$$\begin{aligned} \mathcal{E}_{\mathbf{u}}(\mathbf{u}, d; \delta \mathbf{u}) &= \int_{\Omega} g(d_+) \tilde{\boldsymbol{\sigma}}^{iso,+}(\mathbf{u}) : \boldsymbol{\varepsilon}(\delta \mathbf{u}) \, d\mathbf{x} + \int_{\Omega} \tilde{\boldsymbol{\sigma}}^{iso,-}(\mathbf{u}) : \boldsymbol{\varepsilon}(\delta \mathbf{u}) \, d\mathbf{x} - \int_{\partial_N \Omega} \bar{\boldsymbol{\tau}} \cdot \delta \mathbf{u} \, ds = 0 \quad \forall \delta \mathbf{u} \in V, \\ \mathcal{E}_d(\mathbf{u}, d; \delta d - d) &= (1 - \kappa) \int_{\Omega} 2d_+ \tilde{D}(\delta d - d) \, d\mathbf{x} \\ &\quad + G_c \int_{\Omega} \left(\frac{1}{l} (d - 1) (\delta d - d) + l \nabla d \cdot \nabla (\delta d - d) \right) \, d\mathbf{x} \geq 0 \quad \forall \delta d \in W \cap L^\infty. \end{aligned} \tag{17}$$

Herein, $\mathcal{E}_{\mathbf{u}}$ and \mathcal{E}_d are the first directional derivatives of the energy functional \mathcal{E} given in Formulation 2.1 with respect to the two fields, i.e., \mathbf{u} and d , respectively. Furthermore, $\delta \mathbf{u} \in \{\mathbf{H}^1(\Omega)^2 : \delta \mathbf{u} = \mathbf{0} \text{ on } \partial \Omega_D\}$ is the deformation test function and $\delta d \in H^1(\Omega)$ is the phase-field test function.

Furthermore, the second-order constitutive stress tensor with respect to Eq. 16 reads

$$\boldsymbol{\sigma}(\boldsymbol{\varepsilon}, d) := \frac{\partial w_{bulk}(\boldsymbol{\varepsilon}, d)}{\partial \boldsymbol{\varepsilon}} = g(d_+) \frac{\partial \tilde{\Psi}^+}{\partial \boldsymbol{\varepsilon}} + \frac{\partial \tilde{\Psi}^-}{\partial \boldsymbol{\varepsilon}} = g(d_+) \tilde{\boldsymbol{\sigma}}^+ + \tilde{\boldsymbol{\sigma}}^-, \tag{18}$$

with

$$\tilde{\boldsymbol{\sigma}}^\pm(\boldsymbol{\varepsilon}) := \lambda I_1^\pm(\boldsymbol{\varepsilon}) \mathbf{I} + 2\mu \boldsymbol{\varepsilon}_\pm. \tag{19}$$

2.6. Crack driving forces for brittle failure

Following [29, 30], we determine the crack driving state function to couple between two PDEs. Hence, crack driving state function acts as a right hand side for the phase-field equation. To formulate the crack driving state function, we consider the crack irreversibility condition, which is the inequality constraint $\dot{d} \leq 0$ imposed on our variational formulation. The first variation of the total pseudo-energy density with respect to the crack phase-field given in (15) reads

$$-\delta_d w(\boldsymbol{\varepsilon}, d, \nabla d) = (\kappa - 1) 2d_+ [\tilde{\Psi}^+] - G_c \delta_d \gamma_l(d, \nabla d) \leq 0. \tag{20}$$

Herein, the functional derivative of $\gamma_l(d, \nabla d)$ with respect to d is

$$\int_{\Omega} \delta_d \gamma_l(d, \nabla d) dx = \int_{\Omega} \frac{1}{l} [(d-1) - l^2 \Delta d] dx. \quad (21)$$

Maximization the inequality given in Eq. 20 with respect to the time history $s \in [0, t_n]$ reads

$$(\kappa - 1)2d_+ \max_{s \in [0, t_n]} [\widetilde{\Psi}^+] = G_c \delta_d \gamma_l(d, \nabla d). \quad (22)$$

We multiply Eq. 22 by $\frac{l}{G_c}$. Then Eq. 22 can be restated as

$$(\kappa - 1)2d_+ \mathcal{H} = l \delta_d \gamma_l \quad \text{if} \quad \mathcal{H} := \max_{s \in [0, t_n]} \widetilde{D} \quad \text{with} \quad \widetilde{D} := \frac{l \widetilde{\Psi}^+}{G_c}. \quad (23)$$

Here, $\mathcal{H} := \mathcal{H}(\varepsilon, t)$ denotes a positive crack driving force that is used as a history field from initial time up to the current time. Note that the crack driving state function \widetilde{D} is affected by the length-scale parameter l and hence depends on the regularization parameter.

- Input:**
- loading data (\bar{u}_n, \bar{t}_n) on $\partial\Omega_D \subset \partial\Omega$,
 - solution $(\mathbf{u}_{n-1}, d_{n-1})$ from time step $n - 1$.

Initialization of alternate minimization scheme ($k = 0$):

- set FLAG:=true

while FLAG **do**

1. set $k := 1$
2. given \mathbf{u}^k , solve $\mathcal{E}_d(\mathbf{u}^k, d; \delta d) = 0$ for d , set $d := d^k$,
3. given d^{k-1} , solve $\mathcal{E}_u(\mathbf{u}, d^{k-1}; \delta \mathbf{u}) = 0$ for \mathbf{u} , set $\mathbf{u} := \mathbf{u}^k$,
4. define alternate minimization residual for the obtained pair (\mathbf{u}^k, d^k)

$$\text{Res}_{\text{Stag}}^k := |\mathcal{E}_d(\mathbf{u}^k, d^k; \delta d)| + |\mathcal{E}_u(\mathbf{u}^k, d^k; \delta \mathbf{u})| \quad \forall \delta \mathbf{u} \in \mathbf{V} \quad \delta d \in W, \quad (24)$$

5. **if** $\text{Res}_{\text{Stag}}^k \leq \text{TOL}_{\text{Stag}}$ **then**

- set $(\mathbf{u}^k, d^k) := (\mathbf{u}_n, d_n)$
- FLAG:=false

else

$$k + 1 \rightarrow k$$

end if

end

Algorithm 1: Alternate minimization scheme for Formulation (2.3) at a fixed loading step n .

Formulation 2.3 (Final Euler-Lagrange equations). *Let us assume that λ, μ are given as well as the initial condition $\mathbf{u}_0 = \mathbf{u}(\mathbf{x}, 0)$ and $d_0 = d(\mathbf{x}, 0)$. For the loading increments $n \in \{1, 2, \dots, N\}$, find $\mathbf{u} := \mathbf{u}^n \in V$ and $d := d^n \in W$ such*

that

$$\begin{aligned}\mathcal{E}_u(\mathbf{u}, d_+; \delta \mathbf{u}) &= \int_{\Omega} g(d_+) \tilde{\boldsymbol{\sigma}}_{\varepsilon}^+(\mathbf{u}) : \boldsymbol{\varepsilon}(\delta \mathbf{u}) \, d\mathbf{x} + \int_{\Omega} \tilde{\boldsymbol{\sigma}}_{\varepsilon}^-(\mathbf{u}) : \boldsymbol{\varepsilon}(\delta \mathbf{u}) \, d\mathbf{x} - \int_{\partial_N \Omega} \bar{\boldsymbol{\tau}} \cdot \delta \mathbf{u} \, ds = 0 \quad \forall \delta \mathbf{u} \in V, \\ \mathcal{E}_d(\mathbf{u}, d; \delta d) &= (1 - \kappa) \int_{\Omega} 2d_+ \mathcal{H} \delta d \, d\mathbf{x} + \int_{\Omega} ((d - 1)\delta d + l^2 \nabla d \cdot \nabla \delta d) \, d\mathbf{x} = 0 \quad \forall \delta d \in W.\end{aligned}\tag{25}$$

The multi-field problem given in Formulation (2.3) depending on \mathbf{u} and d implies alternately fixing \mathbf{u} and d , which is a so called alternate minimization scheme, and then solving the corresponding equations until convergence. The alternate minimization scheme applied to the Formulation (2.3) is summarized in Algorithm 1.

3. Uncertainty quantification

In this section, we explain the source of uncertainty in phase-field models. Then, we introduce a computationally effective numerical technique to estimate the unknown parameters.

In the phase-field model, the uncertainty arises from the Lamé parameters including the shear modulus μ and Lamé's first parameter λ as well as Griffith's critical elastic energy release rate (material stiffness parameter) G_c , which are assumed to be random fields. We represent the uncertainty by a spatially-varying Gamma random field. The field Θ can be characterized by its expectation and covariance using a Karhunen-Loève expansion (KLE). Considering the probability density function \mathbb{P} , the expansion is

$$\text{Cov}_{\Theta}(\mathbf{x}, \mathbf{y}) = \int_{\Omega} (\Theta(\mathbf{x}, \omega) - \bar{\Theta}(\mathbf{x})) (\Theta(\mathbf{y}, \omega) - \bar{\Theta}(\mathbf{y})) \, d\mathbb{P}(\omega),\tag{26}$$

which leads to the decomposition

$$\Theta(\mathbf{x}, \omega) = \bar{\Theta}(\mathbf{x}) + \sum_{n=1}^{\infty} \sqrt{\psi_n} k_n(\mathbf{x}) \xi_n(\omega).\tag{27}$$

Here the first term is the mean value, k_n are the orthogonal eigenfunctions, ψ_n are the corresponding eigenvalues of the eigenvalue problem [31]

$$\int_D \text{Cov}_{\Theta}(\mathbf{x}, \mathbf{y}) k_n(\mathbf{y}) \, d\mathbf{y} = \psi_n k_n(\mathbf{x}),\tag{28}$$

and the $\{\xi_n(\omega)\}$ are mutually uncorrelated random variables satisfying

$$\mathbb{E}[\xi_n] = 0, \quad \mathbb{E}[\xi_n \xi_m] = \delta_{nm},\tag{29}$$

where \mathbb{E} indicates the expectation of the random variables.

The infinite series can be truncated to a finite series expansion (i.e., an N_{KL} -term truncation) by [31]

$$\Theta(\mathbf{x}, \omega) = \bar{\Theta}(\mathbf{x}) + \sum_{n=1}^{N_{\text{KL}}} \sqrt{\psi_n} k_n(\mathbf{x}) \xi_n(\omega).\tag{30}$$

For the Gaussian random field, we employ an exponential covariance kernel as

$$\text{Cov}_{\Theta}(\mathbf{x}, \mathbf{y}) = \sigma^2 \exp\left(-\frac{\|\mathbf{x} - \mathbf{y}\|}{\zeta}\right),\tag{31}$$

where ζ is the correlation length as well as σ is the standard deviation.

For a random field, we describe the parameters using an KL-expansion. Considering the Gaussian field $\xi(\mathbf{x})$, a lognormal random field can be generated by the transformation $\tilde{\xi}(\mathbf{x}) = \exp(\xi(\mathbf{x}))$. For instance, for the parameter λ , the truncated KL-expansion can be written as

$$\tilde{\xi}_\lambda(\mathbf{x}, \omega) = \exp\left(\bar{\xi}_\lambda(\mathbf{x}, \omega) + \sum_{n=1}^N \sqrt{\psi_n} k_n(\mathbf{x}) \xi_n(\omega)\right). \quad (32)$$

3.1. Bayesian inference

We consider Formulation (2.3) as the forward model $\mathbf{y} = \mathcal{G}(\Theta(\mathbf{x}))$, where $\mathcal{G}: L^2(\Omega) \rightarrow L^2(\Omega)$. The forward model explains the response of the model to different influential parameters Θ (here μ , λ , and G_c). We can write the statistical model in the form [32]

$$\mathcal{M} = \mathcal{G}(\Theta) + \varepsilon, \quad (33)$$

where \mathcal{M} indicates a vector of observations (e.g., measurements). The error term ε arises from uncertainties such as measurement error due experimental situations. More precisely, it is due to the modeling and the measurements and is assumed to have a Gaussian distribution of the form $\mathcal{N}(0, H)$ with known covariance matrix H . The error is independent and identically distributed and independent from the realizations. Here, for sake of simplicity, we assume $H = \sigma^2 I$ (for a positive constant σ^2).

For a realization θ of the random field Θ corresponding to a realization m of the observations \mathcal{M} , the posterior distribution is given by

$$\pi(\theta|m) = \frac{\pi(m|\theta)\pi_0(\theta)}{\pi(m)} = \frac{\pi(m|\theta)\pi_0(\theta)}{\int_{W_m} \pi(m|\theta)\pi_0(\theta) d\theta}, \quad (34)$$

where $\pi_0(\theta)$ is the prior density (prior knowledge) and W_m is the space of parameters m (the denominator is a normalization constant) [33]. The likelihood function can be defined as [32]

$$\pi(m|\theta) := \frac{1}{(2\pi\sigma^2)^{\bar{n}/2}} \exp\left(-\sum_{n=1}^{\bar{n}} \frac{(m_n - \mathcal{G}(\theta))^2}{2\sigma^2}\right). \quad (35)$$

As an essential characteristic of the phase-field model, the load-displacement curve (i.e., the global measurement) in addition to the crack pattern (i.e., the local measurement) are appropriate quantities to show the crack propagation as a function of time. Figure 3 indicates the load-displacement curve during the failure process. Three major points are the following.

①First stable position. This point corresponds to the stationary limit such that we are completely in elastic region ($d(\mathbf{x}, 0) = 1 \forall \mathbf{x} \in \Omega \setminus C$).

②First peak point. Prior to this point crack nucleation has occurred and now we have crack initiation. Hence, this peak point corresponds to the critical load quantity such that the new crack surface appears (i.e., there exist some elements which have some support with $d = 0$).

③ **Failure point.** At this point failure of the structure has occurred and so increasing the load applied to the material will not change the crack surface anymore.

The interval between point 1 and point 2 in Figure 3 typically refers to the primary path where we are almost in the elastic region. The secondary path (sometimes referred to as the softening path) starts with crack initiation occurring at point 2. The whole process recapitulates the load-deflection curve in the failure process.

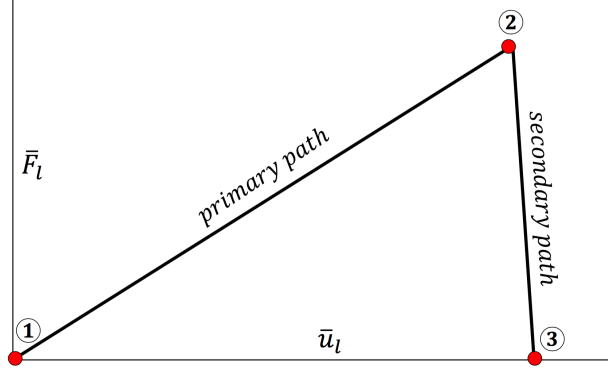


Figure 3: The schematic of load-deflection response for the failure process including primary path (prior to the crack initiation, i.e., between point 1 and 2) and secondary path (during crack propagation, i.e., between point 2 and 3).

The main aim of solving the inverse problem followed here is to determine the random field Θ to satisfy (33). We strive to find a posterior distribution of suitable values of the parameters μ , λ , and G_c in order to match the simulated values (arising from (25)) with the observations. The distribution provides all useful statistical information about the parameter.

Remark 3.1. Note that the principal parameters h , κ , and l are linked. Specifically, $h := \kappa(h)$ and $h := l(h)$ hold such that $h \ll l$ and $h \ll \kappa$ through discretization error estimates. A simplified analysis for a decoupled, linearized, problem is provided in [6], and we set $l = ch^\beta$ with $0 < \beta < \frac{1}{2}$ and $\kappa = ch^\chi$ with $0 < \chi < 1$. Hence, the equations to be solved through Formulation 2.3 are strongly related to the element size h , i.e., the degradation function $g(d_+)$ for displacement equation the and crack driving state \tilde{D} in the phase-field equation. Hence, to resolve the crack phase-field which also tends to the sharp crack surface, a sufficiently small h is chosen to obtain the reference solution (due to the lankness of the experiments). We also notice that from a theoretical side, the inequality $\kappa \ll l$ should hold, which can be justified through Γ convergence results, see e.g., [3, 4].

The crack pattern is a time-dependent process (more precisely in a quasi-static regime, the cracking process is load-dependent), i.e., after initiation it is propagated through time. In order to approximate the parameters precisely, we estimate the likelihood during all time steps. Therefore, the posterior distribution maximizes the likelihood function for all time steps, and therefore we have an exacter curve for all crack nucleation and propagation times.

MCMC is a suitable technique to calculate the posterior distribution. When the parameters are not strongly

correlated, the MH algorithm [34] is an efficient computational technique among MCMC methods. We propose a new candidate (a value of (μ, λ, G_c)) according to a proposal distribution and calculate its acceptance/rejection probability. The ratio indicates how likely the new proposal is with regard to the current sample. In other words, by using the likelihood function (35), the ratio determines whether the proposed value is accepted or rejected with respect to the observation (here the solution of Formulation 2.3 with a very fine mesh). As mentioned, fast convergence means that the parameters are uncorrelated. A summary of the MH algorithm is given below.

Initialization: set prior data θ^0 and number of samples N .

for $\ell = 1 : N$ **do**

1. Propose a new candidate based on the proposal distribution $\theta^* \sim \mathcal{K}(\theta^* | \theta^{\ell-1})$.
2. Compute the acceptance/rejection probability $\nu(\theta^* | \theta^{\ell-1}) = \min \left(1, \frac{\pi(\theta^* | m)}{\pi(\theta^{\ell-1} | m)} \frac{\mathcal{K}(\theta^{\ell-1} | \theta^*)}{\mathcal{K}(\theta^* | \theta^{\ell-1})} \right)$.
3. Generate a random number $\mathcal{V} \sim \text{U}(0, 1)$.
4. **if** $\mathcal{V} < \nu$ **then**
 accept the proposed candidate θ^* and set $\theta^\ell := \theta^*$
else
 reject the proposed candidate θ^* and set $\theta^\ell := \theta^{\ell-1}$
end if

end

Algorithm 2: The Metropolis-Hastings algorithm.

4. Bayesian inversion for phase-field fracture

In this key section, we combine the phase-field algorithm from Section 2 with the Bayesian framework presented in Section 3.

First, we define two sampling strategies as follows:

- *One-dimensional* Bayesian inversion. We first use N -samples (according to the proposal distribution) and extract the posterior distribution of the first unknown (e.g., μ) where other parameters are according to the mean value. Then obtained information is used to estimate the posterior distribution of next unknowns (e.g., λ); where here still G_c is according to the mean. Finally, the expected value of obtained parameters (here μ and λ) will be employed in the Bayesian inference (see Algorithm 2) to estimate G_c .
- *Multi-dimensional* Bayesian inversion. A three-dimensional candidate $(\mu^\ell, \lambda^\ell, G_c^\ell)$, as i -th candidate) is proposed (based on the proposal distribution) and the algorithm computes its acceptance/rejection probability.

To make the procedures more clarified we explain the multi-dimensional approach in Algorithm 3. Clearly, for the one-dimensional setting; for each parameter (e.g., $\theta = \mu$), it can be reproduced separately. We will study both techniques in the first example and the more efficient method will be used for other simulations.

```

for  $\ell = 1 : N$  do
  1. Propose the  $\ell$ -th candidate  $\theta^* = (\mu^*, \lambda^*, G_c^*)$  according to the proposal distribution (uniform or normal).
  2. • set FLAG=true
      • set  $n = 0$ 
  while FLAG do
    (i) solve the Formulation (2.3) by Algorithm 1 considering TOLStag and
        the proposed candidate  $\theta^*$ .
    (ii) approximate  $(\mathbf{u}_n, d_n)$ 
    (iii) estimate the crack pattern at the loading stage  $n$  by
        
$$\bar{F}_n = \int_{\partial\Omega_D} \mathbf{n} \cdot \boldsymbol{\sigma} \cdot \mathbf{n} \, d\mathbf{x} \quad (36)$$

    (iv) if  $\left\{ \exists d = 0 \text{ in } \Omega \setminus C \right\} \& \left\{ \|\bar{F}_n\| < \text{TOL}_{\text{Load}} \right\}$  or  $n < n_{\max}$  then
      • set FLAG=false
    else
      • set  $n = n + 1$ 
    end if
  end
  3. Calculate the likelihood function (35) for  $\bar{F}$  (during all  $n$ -steps, until  $\bar{n}$ ) with respect to  $\theta^*$  where  $m_n$ 
    indicates the reference value at the  $n$ -th loading step.
  4. Compute the acceptance/rejection probability  $\nu(\theta^* | \theta^{\ell-1})$ .
  5. Use Algorithm 2 to determine  $\theta^\ell$  (i.e.,  $\theta^*$  is accepted/rejected).
end

```

Algorithm 3: The multi-dimensional Bayesian inversion for phase-field fracture.

Here, n_{\max} is the sufficiently large value that is set by the user. Also, TOL_{Load} is a sufficiently small value to guarantee that the crack phase-field model reached to the material failure time. Note, in part (iv) for the while-loop step, the criteria $\|\bar{F}_n\| < \text{TOL}_{\text{Load}}$ in the secondary path (i.e., during crack propagation state) guarantees that reaction force under imposed Dirichlet boundary surface is almost zero. Hence, no more force exists to produce a fractured state. We now term this as a complete failure point. But, in some cases, e.g., shear test as reported in [28], by increasing the monotonic displacement load, \bar{F}_n is not reached to zero. For this type of problem, if $n < n_{\max}$ holds then phase-field step (i.e., while-loop step) in Algorithm 3 will terminate.

5. Numerical examples

In this section we consider numerical test problems to determine the unknown parameters using given Bayesian inference. Specifically, we investigate:

- Example 1. the single edge notch tension (SENT) test;
- Example 2. double edge notch tension (DENT) test;
- Example 3. tension test with two voids.

The observations can be computed by very fine meshes (here the reference values) as an appropriate replacement of the measurements (see Remark 3.1). Regarding the observational noise, $\sigma^2 = 1 \times 10^{-3}$ is assumed. The main aim here is to estimate the effective parameters (μ , λ , and G_c) in order to match the load-displacement curve with the reference value. Furthermore, we assume that there is no correlation between μ , λ , and G_c . To characterize the random fields, we can use the KL-expansion with $N_{\text{KL}} = 100$ and the correlation length $\zeta = 2$ as well.

The phase-field parameters set by $\kappa = 10^{-8}$, and regularized length scale $l = 2h$ (respecting the condition $h < l$). The stopping criterion for the iterative Newton method scheme, i.e. the relative residual norm that is

$$\text{Residual} := \|\mathbf{R}(\mathbf{x}_{k+1})\| \leq \text{To1}_{\text{N-R}} \|\mathbf{R}(\mathbf{x}_k)\|, \quad (37)$$

is chosen to $\text{To1}_{\text{N-R}} = 10^{-8}$. Here, \mathbf{R} indicates a discretized setting of weak forms described in Formulation (2.3). Regarding alternate minimization scheme we set $\text{TOL}_{\text{stag}} = 10^{-4}$ for all numerical examples. Finally $\text{TOL}_{\text{Load}} = 10^{-3}$ is chosen to guarantee that the we solve the model only until the material failure time.

5.1. Example 1. The single edge notch tension (SENT) test

This example considers the single edge notch tension. The specimen is fixed at the bottom. We have traction-free conditions on both sides. A non-homogeneous Dirichlet condition is applied at the top. The domain includes a predefined single notch (as an initial crack state imposed on the domain) from the left edge to the body center, as shown in Figure 4a. We set $A = 0.5$ mm hence $\Omega = (0, 1)^2 \text{mm}^2$, hence the predefined notch is in the $y = A$ plane and is restricted to $0 \leq |C| \leq A$. This numerical example is computed by imposing a monotonic displacement $\bar{u} = 1 \times 10^{-4}$ at the top surface of the specimen in a vertical direction. The finite element discretization corresponding to $h = 1/80$ is indicated in Figure 4b.

For the shear modulus, we assume the variation range (60 kN/mm^2 , 100 kN/mm^2). Regarding the Lamé modulus λ , the parameter varies between 100 kN/mm^2 and 140 kN/mm^2 . Finally, we consider the interval between $2.1 \times 10^{-3} \text{ kN/mm}^2$ and $3.3 \times 10^{-3} \text{ kN/mm}^2$ for G_c .

We solved the PDE model (Formulation 2.3) with $\lambda = 120 \text{ kN/mm}^2$, $\mu = 80 \text{ kN/mm}^2$, and $G_c = 2.7 \times 10^{-3} \text{ kN/mm}^2$ [28] and the displacement during the time (as the reference solution) with $h = 1/320$ was obtained. The main goal is to obtain the suitable values of μ , λ , and G_c such that the simulations match the reference value.

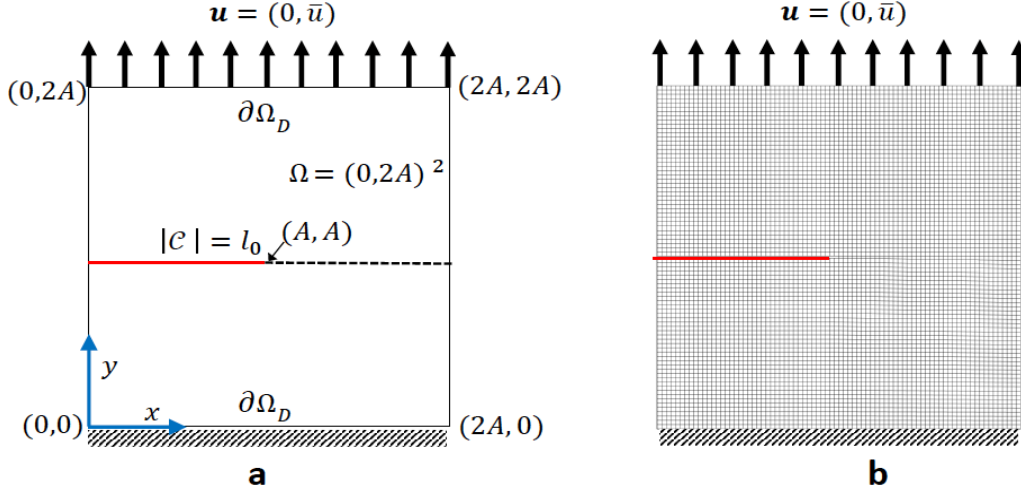


Figure 4: Schematic of SENT (Example 1) (left) and its corresponding mesh with $h = 1/80$ (right).

	one-dimensional		three-dimensional	
	mean (kN/mm ²)	ratio (%)	mean (kN/mm ²)	ratio (%)
μ	84.1	24	85	24.5
λ	120.2	30.3	119.1	30
G_c	0.00273	29	0.00269	28.5

Table 1: The mean values of the posterior distributions obtained by one-dimensional and three-dimensional Bayesian inversion in addition to their acceptance ratios for the SENT (Example 1). The units are in kN/mm².

For this example, we use a uniformly distributed prior distribution and the symmetric proposal distribution [35]

$$\mathcal{K}(\theta \rightarrow \theta^*) := \frac{1}{\theta_2 - \theta_1} \chi[\theta_1, \theta_2](\theta), \quad (38)$$

where χ indicates the characteristic function of the interval $[\theta_1, \theta_2]$.

First, we describe the effect of each parameter on the displacement. As the Lamé constants (i.e., μ and λ) become larger, the material response becomes stiffer; crack initiation takes longer to occur. Additionally, a larger crack release energy rate (as an indicator for the material resistance against the crack driving force) delays crack nucleation and hence crack dislocation. All these facts are illustrated in Figure 5.

The posterior distributions obtained by both one- and three-dimensional Bayesian inversions are shown in Figure 6. The mean values of the distributions are $\mu = 84.1$ kN/mm² and $\mu = 85$ kN/mm², and the acceptance rates are 24% and 24.5%, respectively. As we already expected (see Figure 5), the 1st parameter Lamé is not as influential as the

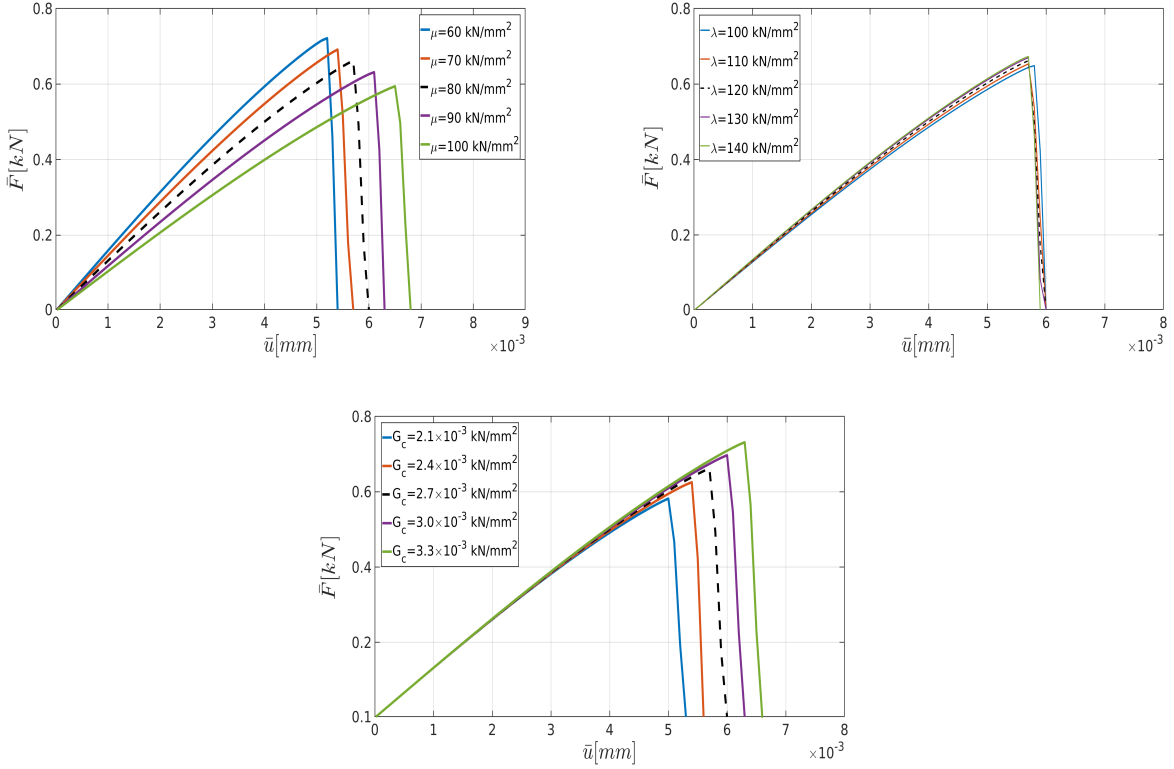


Figure 5: The force/displacement curve for different values of μ (top left), λ (top right) and G_c (bottom) in the SENT example (Example 1).

shear modulus. This fact is validated by the posterior distribution, where wider distributions (with higher acceptance rates, approximately 30%) are obtained. Regarding the material stiffness parameter G_c , the acceptance rates are near 29%. The values are summarized in Table 1.

To verify the parameters obtained by the Bayesian approach, we solved the forward model using the mean values of the posterior distributions. Figure 7 shows the load-displacement diagram according to prior and posterior distributions. As expected, during the nucleation and propagation process, using Bayesian inversion results in better agreement (compared to the prior). Furthermore, a better estimation is achieved by simultaneous *multi-dimensional* Bayesian inversion. From now onward, this approach will be used for Bayesian inference.

5.1.1. The convergence of MCMC

A customary method to assess the convergence of the MCMC is the calculation of its autocorrelation. The lag- τ autocorrelation function (ACF) $R: \mathbb{N} \rightarrow [-1, 1]$ is defined as

$$R(\tau) := \frac{\sum_{n=1}^{N-\tau} (\theta_n - \bar{\theta})(\theta_{n+\tau} - \bar{\theta})}{\sum_{n=1}^N (\theta_n - \bar{\theta})^2} = \frac{\text{cov}(\theta_n, \theta_{n+\tau})}{\text{var}(\theta_n)},$$

where θ_n is the n -th element of the Markov chain and $\bar{\theta}$ indicates the mean value. For the Markov chains, $R(\tau)$ is positive and strictly decreasing. Also, a rapid decay in the ACF indicates the samples are uncorrelated and mixing

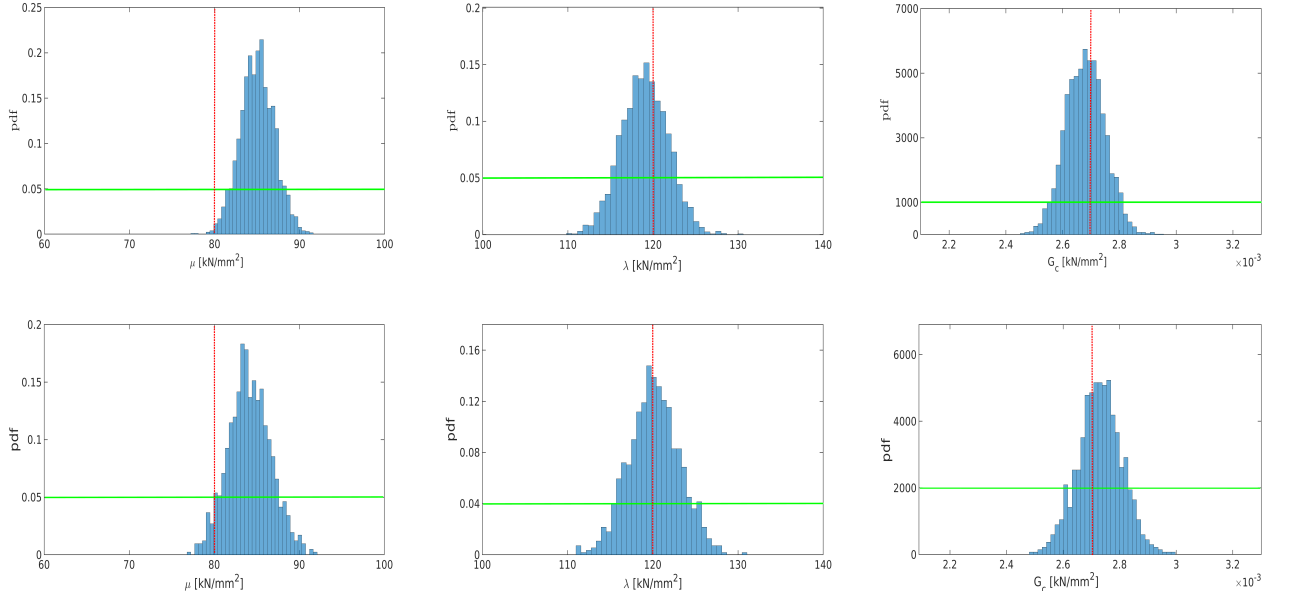


Figure 6: The prior (green line), the mean value (red line), and the normalized probability density function (pdf) of posterior distribution of μ (top left), λ (top right) and G_c (bottom) for the SENT example. Here we compare the distributions obtained by the three-dimensional Bayesian inversion (first row) and the one-dimensional Bayesian inversion (second row).

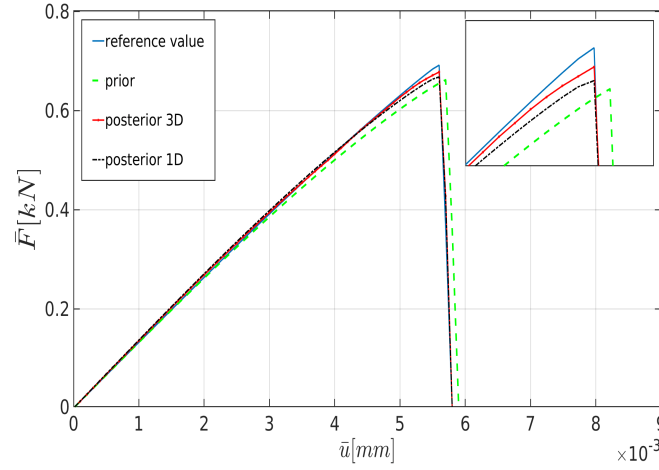


Figure 7: The load-displacement curve for the one-dimensional (black) and three-dimensional (red) posterior distributions in addition to the ones for the prior distribution (green) and the reference value (blue) for the SENT example (Example 1) with $h = 1/160$.

well. Figure 8 shows the convergence of the MCMC where the Lamé constants and the critical elastic energy release rate are estimated with the one-dimensional MH algorithm. Also, we estimated the convergence observed in the multi-dimensional approach. For all parameters, MCMC converges fast indicating that they are not correlated. As expected, the multi-dimensional approach converges slower than the one-dimensional one.

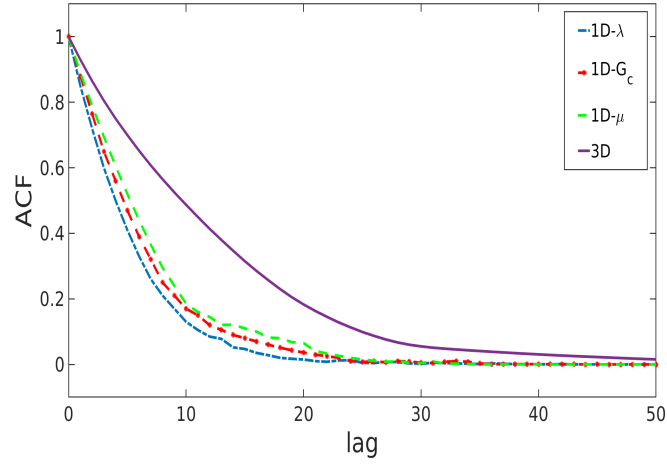


Figure 8: The autocorrelation function for one- and multidimensional Bayesian inference in the SENT example (Example 1).

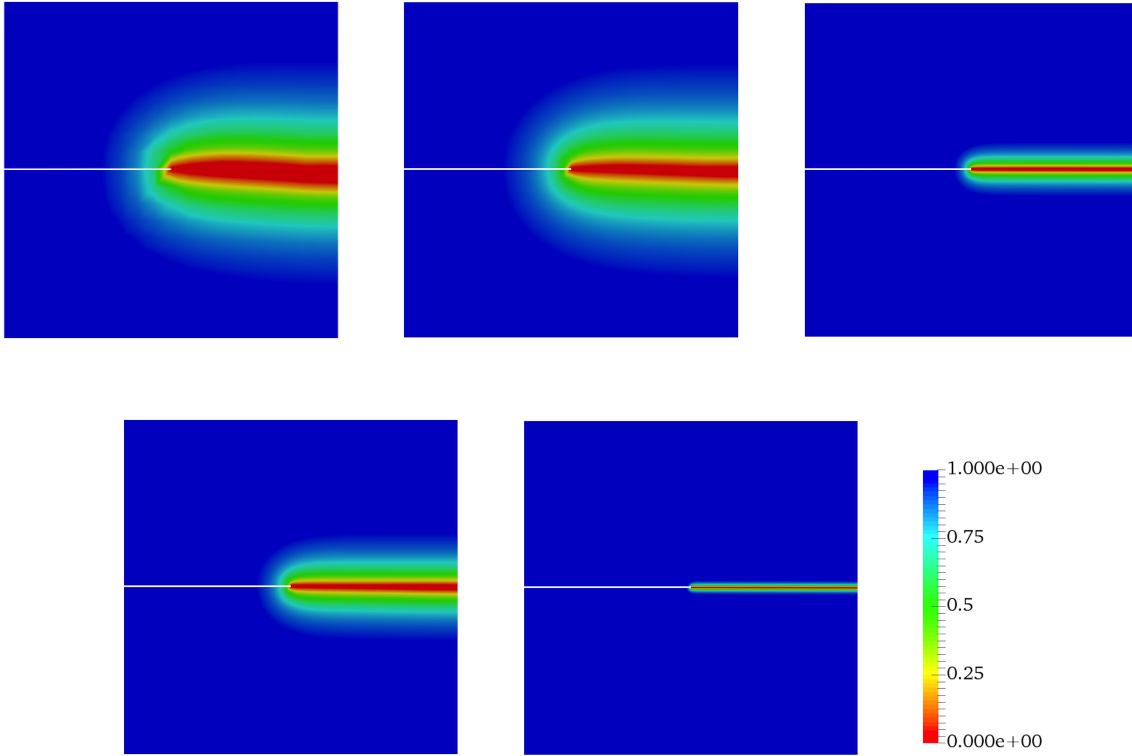


Figure 9: The effect of the mesh size on the crack propagation in the SENT example (Example 1). The mesh sizes are (from the left) $h = 1/20$, $h = 1/40$, $h = 1/80$, $h = 1/160$, and $h = 1/320$ (the reference). The effective parameters are chosen according to the prior values.

As noted above, the phase-field solution depends on h and l . A detailed computational analysis was for instance performed in [7, 8]. In general, for smaller h (and also smaller l) the crack path is better resolved, but leads to a much higher computational cost.

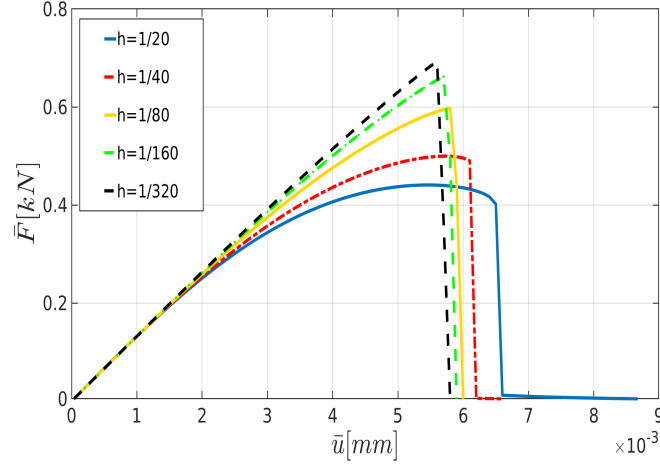


Figure 10: The load-displacement curve of in the SENT example (Example 1) for different mesh sizes, where the parameters are chosen according to the prior.

Figure 9 illustrates the crack pattern using different mesh sizes varying between $h = 1/20$ and $h = 1/320$. For these mesh sizes, we also show the load-displacement diagram in Figure 10.

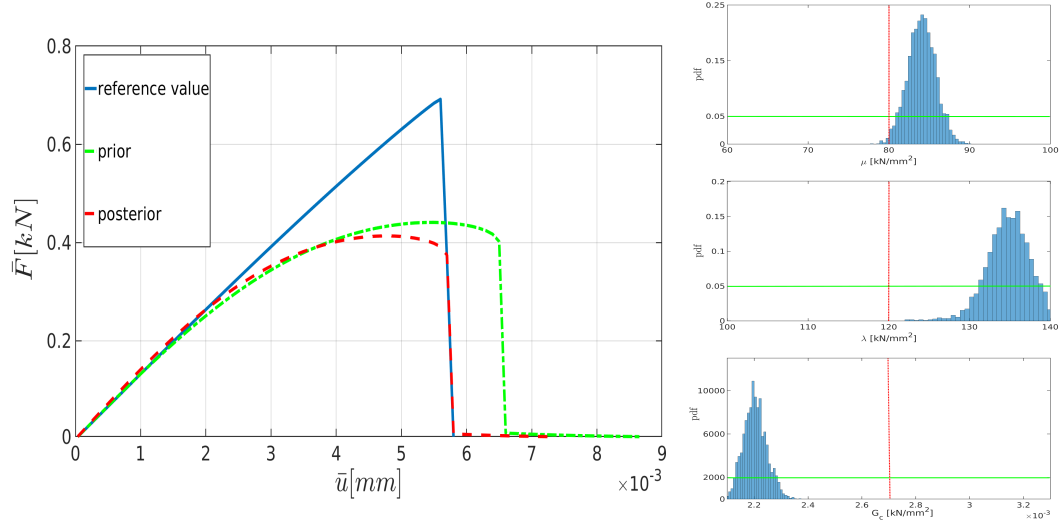


Figure 11: The load-displacement curves for the reference, prior, and posterior values (left panel) for $h = 1/20$ in the SENT example (Example 1). The marginal posterior distributions of the effective parameters are shown in the right panel.

Here we strive to solve the problem using a coarse mesh and employ MCMC to find parameters that make the solution more precise compared with the reference value. Figure 11 shows the obtained displacement with both prior and posterior distribution for $h = 1/20$. The efficiency of the Bayesian estimation is pointed out here since the peak point and the failure point are estimated precisely. The marginal posterior distributions are shown in the right panel as well. The estimation can also be performed for finer meshes: Figure 12 and Figure 13 illustrate the load-

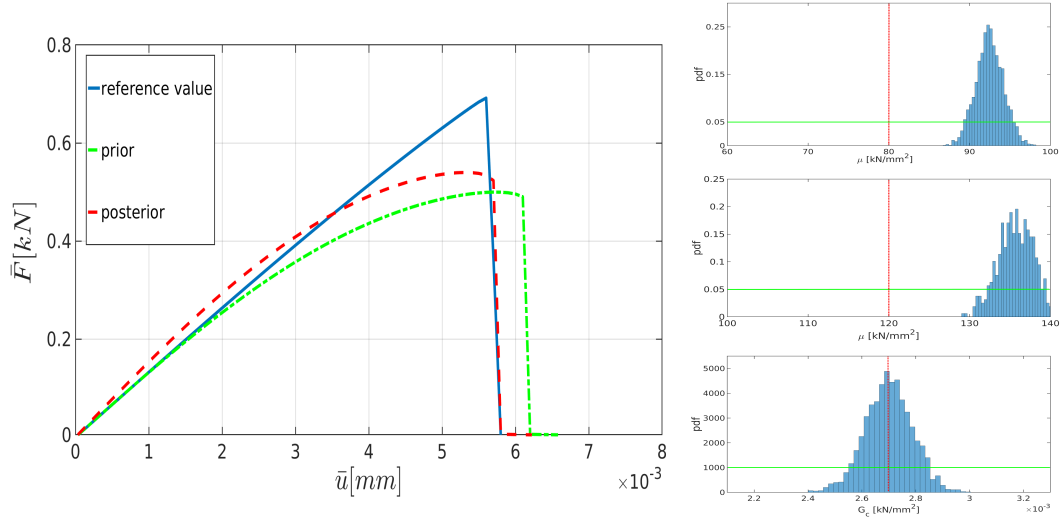


Figure 12: The load-displacement curves for the reference, prior, and posterior values (left panel) for $h = 1/40$ in the SENT example (Example 1). The marginal posterior distributions of the effective parameters are shown in the right panel.

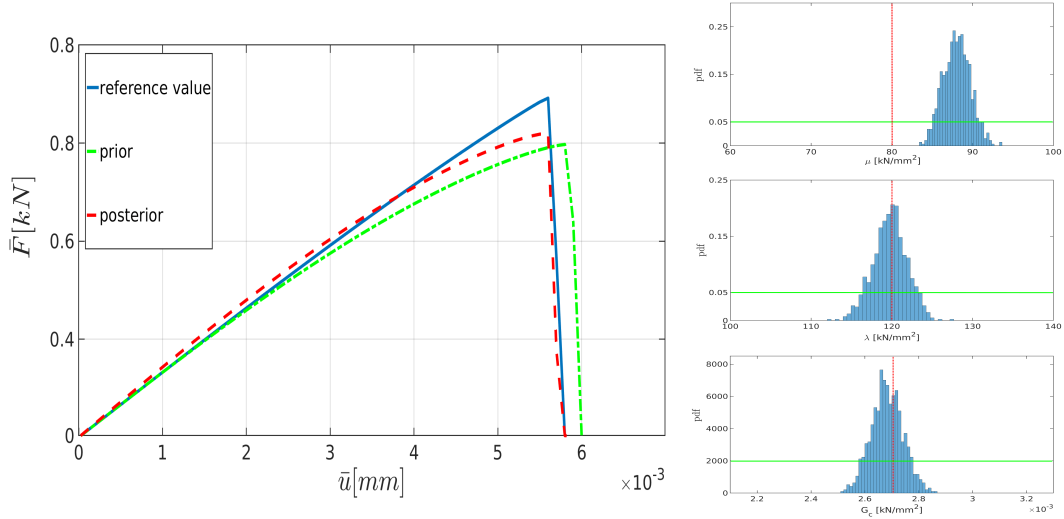


Figure 13: The displacement curves for the reference, prior, and posterior values (left panel) for $h = 1/80$ in the SENT example (Example 1). The marginal posterior distributions of the effective parameters are shown in the right panel.

displacement curves for $h = 1/40$ and $h = 1/80$, respectively. In both cases, in addition to the precise estimation of the crack-initiation point and the material-failure point, the curve is closer to the reference value. Again, the posterior distributions are shown on the right panels. Finally, the mean values of the posterior distributions in addition to their acceptance rates are indicated in Table 2.

	μ	rate (%)	λ	rate (%)	G_c	rate (%)
$h = 1/20$	84.0	24	134.5	15	0.00220	20
$h = 1/40$	92.5	26	136.1	16	0.00270	25
$h = 1/80$	88.0	25	119.8	28	0.00268	28

Table 2: The mean of the marginal posterior distributions of μ , λ , and G_c in the SENT example (Example 1) for $h = 1/20$, $h = 1/40$, and $h = 1/80$. All units are in kN/mm^2 .

5.2. Example 2. Double edge notch tension (DENT) test

This numerical example is a fracture process that occurs through the coalescence and merging of two cracks in the domain. We consider the tension test with a double notch located on the left and right edge. The specimen is fixed on the bottom. We have traction-free conditions on both sides. A non-homogeneous Dirichlet condition is applied to the top-edge. The domain has a predefined two-notch located in the left and right edge in the body as shown in Figure 14a. We set $A := 20 \text{ mm}$ and $B := 10 \text{ mm}$ hence $\Omega = (20, 10)^2 \text{ mm}^2$. For the double-edge-notches, let $H_1 := 5.5 \text{ mm}$ and $H_2 := 3.5 \text{ mm}$ with the predefined crack length of $l_0 := 5 \text{ mm}$ (Figure 14a). This numerical example is computed by imposing a monotonic displacement $\bar{u} = 1 \times 10^{-4}$ at the top surface of the specimen in a vertical direction. The finite element discretization uses $h = 1/80$ is indicated in Figure 14b.

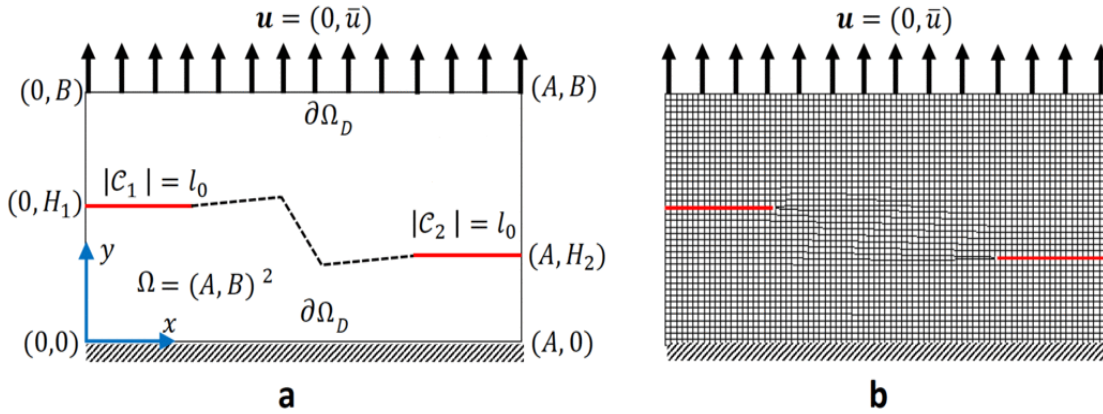


Figure 14: Schematic diagram for the DENT example (Example 2) (left) and its corresponding mesh with $h = 1/80$ (right).

According to the truncated KL-expansion, for the Lamé modulus λ , Eq. 32 gives the mean value of $\bar{\lambda} = 23.2$ and the standard deviation of $\sigma_\lambda = 0.16$. Therefore, the parameter varies between 10 kN/mm^2 and 14 kN/mm^2 . For the shear modulus, the expectation of $\bar{\mu} = 22.8$ and the standard deviation of $\sigma_\mu = 0.23$ leads to the variation range $(6 \text{ kN/mm}^2, 10 \text{ kN/mm}^2)$. Similarly, by using a KL-expansion for G_c , we obtained the variation range between $8 \times 10^{-5} \text{ kN/mm}^2$ and $12 \times 10^{-5} \text{ kN/mm}^2$. Figure 15 illustrates the effect of their different values on the curve, where

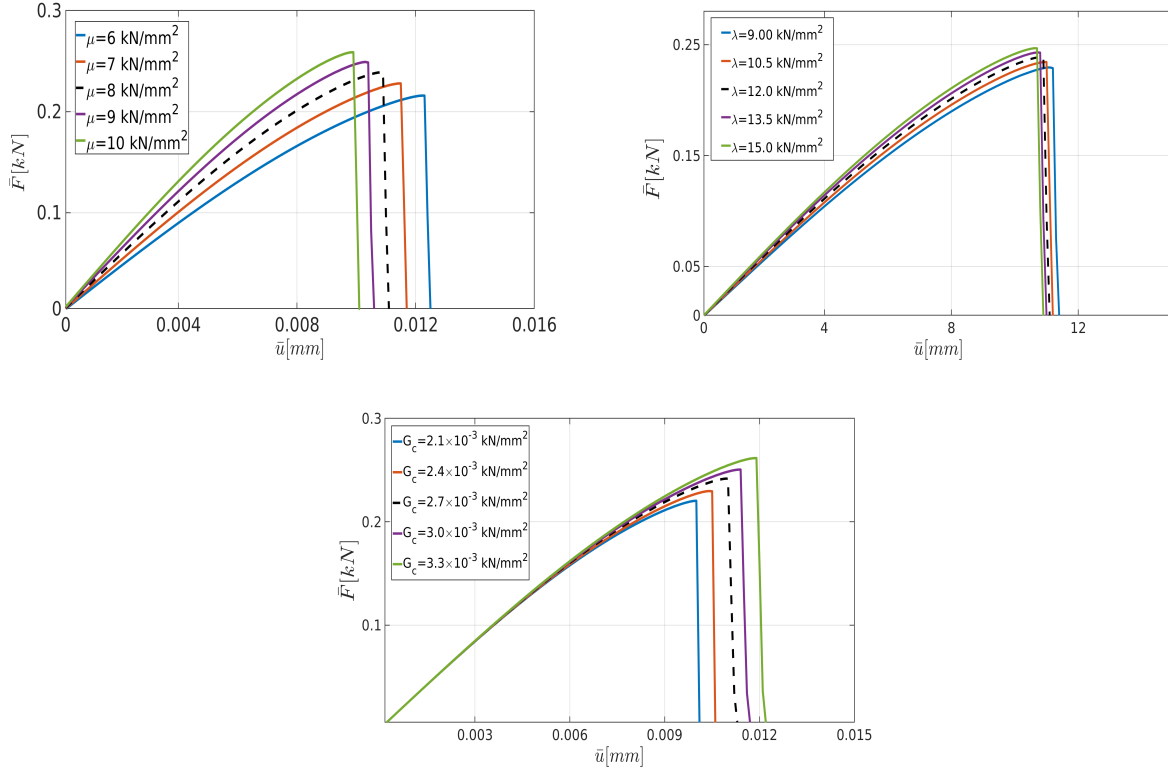


Figure 15: The force/displacement curve for different values of μ (top left), λ (top right) and G_c (bottom) for the DENT example (Example 2).

similar to SENT the influence of the shear modulus and material stiffness parameter is larger than the Lamé modulus.

We assumed the symmetric proposal distribution, namely the normal distribution

$$\mathcal{K}(\theta \rightarrow \theta^*) := \frac{1}{\sqrt{2\pi\sigma^2}} \exp\left(-\frac{(\theta - \theta^*)^2}{2\sigma^2}\right). \quad (39)$$

Here we plan to study the effect of the number of samples N on the posterior distribution. Figure 16 shows the distributions of λ , μ , and G_c in addition to their prior distribution using $N = 3000$, $N = 12000$, and $N = 50000$. The calculations are done with $h = 1/80$, and $h = 1/320$ is used as the reference. As shown, with a larger number of samples, the distribution is close to a normal distribution. Table 3 points out the mean values in addition to the acceptance rate. For both Lamé constants, the suitable chosen prior distribution gives rise to a higher acceptance rate (more than 30% for all candidates). However, for G_c , the candidates tend to lower values (to converge more to the reference value), and therefore more candidates are rejected (around 15% acceptance rate). Table 3 summarizes the mean values of the posterior distributions of all influential parameters.

As the next step, we use different mesh sizes for the Bayesian inversion. Figure 17 shows the crack pattern using different mesh sizes changing from $h = 1/10$ to $h = 1/320$. Finer meshes lead to a smoother and more reliable pattern. Figure 18 depicts the load-displacement diagram using the prior values. With coarse meshes, the curve is significantly different from the reference including crack initiation. Using Bayesian inversion (see Figure 16) enables

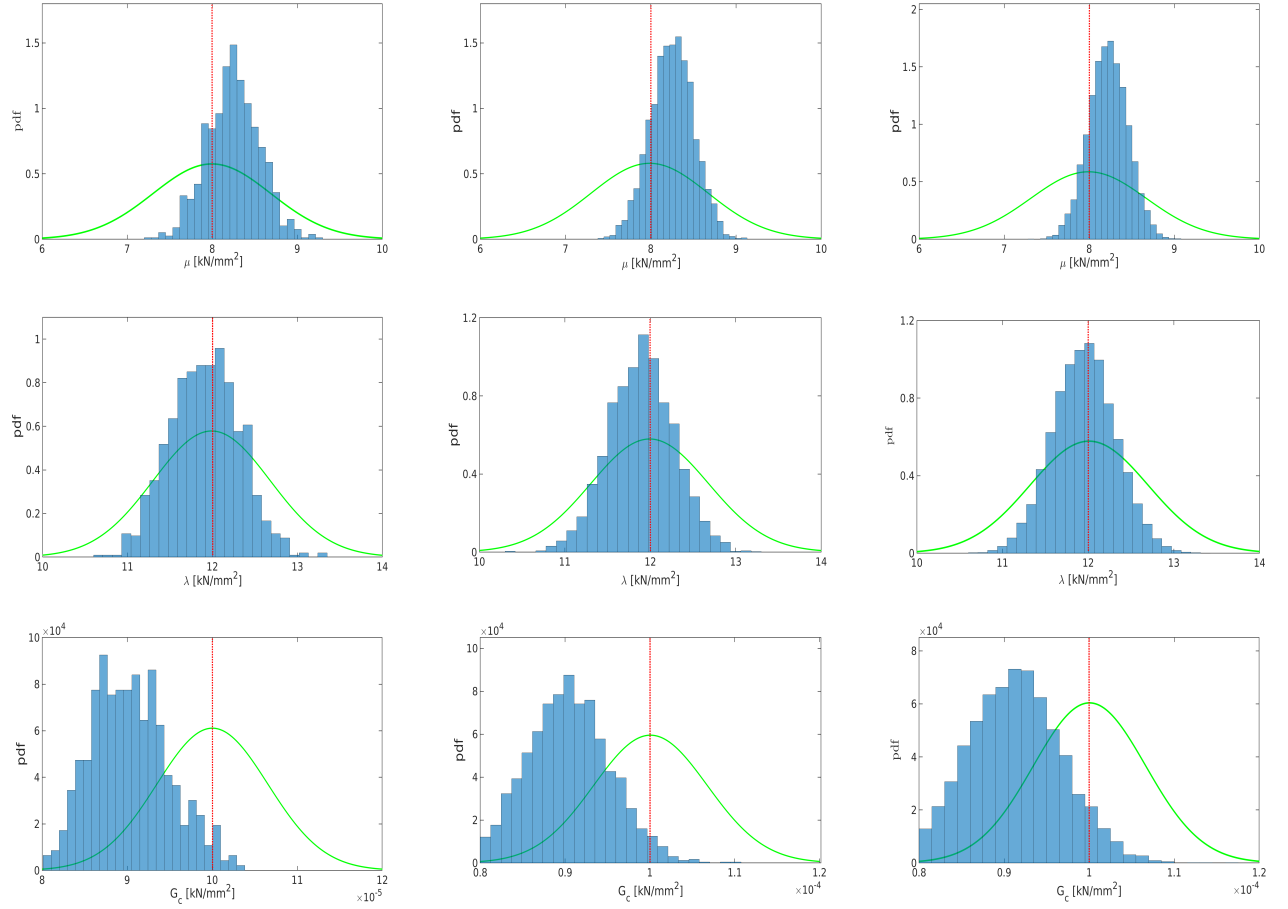


Figure 16: The prior (green curve), the mean value (red line), and posterior (histogram) distribution of μ (the first line), λ (the second line) and G_c (the third line) for the DENT example (Example 2). For the posterior distribution, we used 3 000 samples (the first column), 15 000 samples (the second column), and 50 000 samples (the third column).

us to predict the crack propagation and initiation more precisely. As the figure shows, even for the coarsest mesh (compare $h = 1/10$ to $h = 1/320$) the peak and fracture points are estimated precisely. For finer meshes (e.g., $h = 1/80$) the diagram is adjusted tangibly compared to the reference value. Finally, a summary of the mean values (of posterior distributions) and their respective acceptance rate is given in Table 4.

The significant advantage of the developed Bayesian inversion is a significant computational cost reduction. As shown, for SENT and DENT, by using Bayesian inference for coarser meshes, the estimated load-displacement curve is very close to the reference values. We should note that the needed CPU time for $h = 1/320$ is approximately 4.5 hours; however the solution with $h = 1/80$ is obtained in less than 10 minutes. This fact pronounces the computational efficiency provided by Bayesian inversion, i.e., obtaining a relatively precise solution in spite of using much coarser meshes.

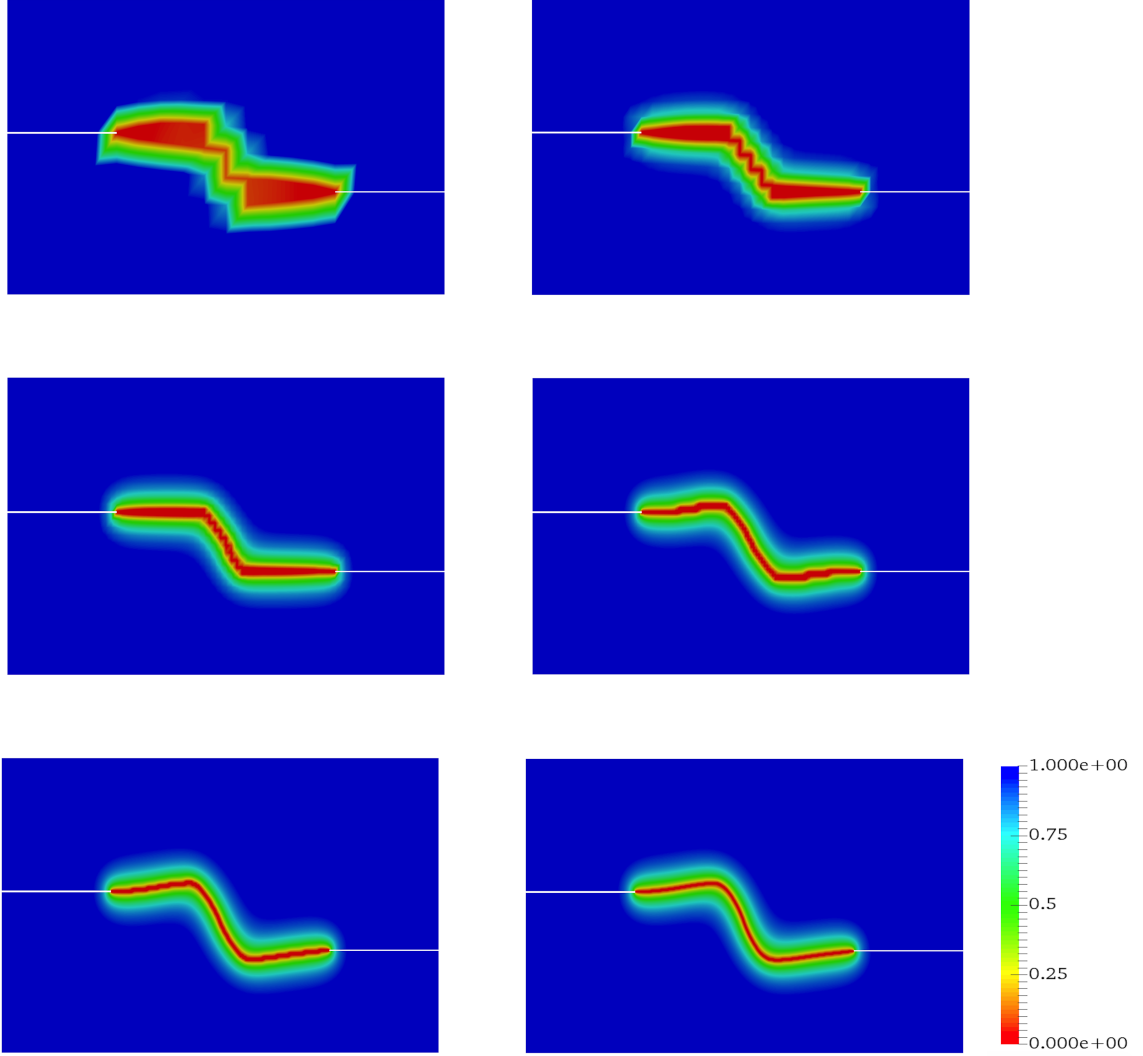


Figure 17: The effect of the mesh size on the crack propagation in the DENT example (Example 2). The mesh sizes are (from the left) $h = 1/10$, $h = 1/20$, $h = 1/40$, $h = 1/80$, $h = 1/160$, and $h = 1/320$ (the reference).

5.3. Example 3. Tension test with two voids

Here we consider the tension test where two voids are located in the domain as a more complicated example. The voids are used to weaken the material and to lead to crack nucleation/initiation without an initial singularity (i.e., a pre-existing crack). The specimen is fixed on the bottom. We have traction-free conditions on both sides. A non-homogeneous Dirichlet condition is applied to the top. Domain includes a predefined two voids in the body, as depicted in Figure 19a. We set $A = 0.5$ mm hence $\Omega = (0, 1)^2$ mm². The radius of left void is $r_1 := 0.247$ with the center $c_1 := (0.21, 0.197)$. The radius of the right void is $r_2 := 0.0806$ with the center $c_2 := (0.7, 0.197)$. This numerical example is computed by imposing a monotonic displacement $\bar{u} := 1 \times 10^{-4}$ at the top surface of the specimen in vertical direction. The finite-element discretization corresponding $h = 1/40$ is shown in Figure 19b.

	$N_{\text{samples}}=3\,000$		$N_{\text{samples}}=15\,000$		$N_{\text{samples}}=50\,000$	
	mean (kN/mm ²)	rate (%)	mean (kN/mm ²)	rate (%)	mean (kN/mm ²)	rate (%)
μ	8.25	31.1	8.22	32.0	8.21	32.8
λ	11.91	31.0	11.93	31.8	11.65	36.2
G_c	9.0×10^{-5}	15.0	9.05×10^{-5}	15.4	9.58×10^{-5}	15.3

Table 3: The mean value and the acceptance rate of the posterior distributions of μ , λ , and G_c with $N_{\text{samples}} = 3\,000$, $N_{\text{samples}} = 12\,000$, and $N_{\text{samples}} = 50\,000$ in the DENT example (Example 2). All units are in kN/mm².

	μ	rate (%)	λ	rate (%)	G_c	rate (%)
$h = 1/20$	8.91	29.0	12.2	37.3	8.11×10^{-5}	11.2
$h = 1/40$	8.11	36.8	12.1	38.2	8.25×10^{-5}	14.2
$h = 1/80$	8.25	34.2	12.0	39.1	9.01×10^{-5}	24.2

Table 4: The mean of the posterior distributions of μ , λ , and G_c for different mesh sizes in the DENT example. The units are in kN/mm²

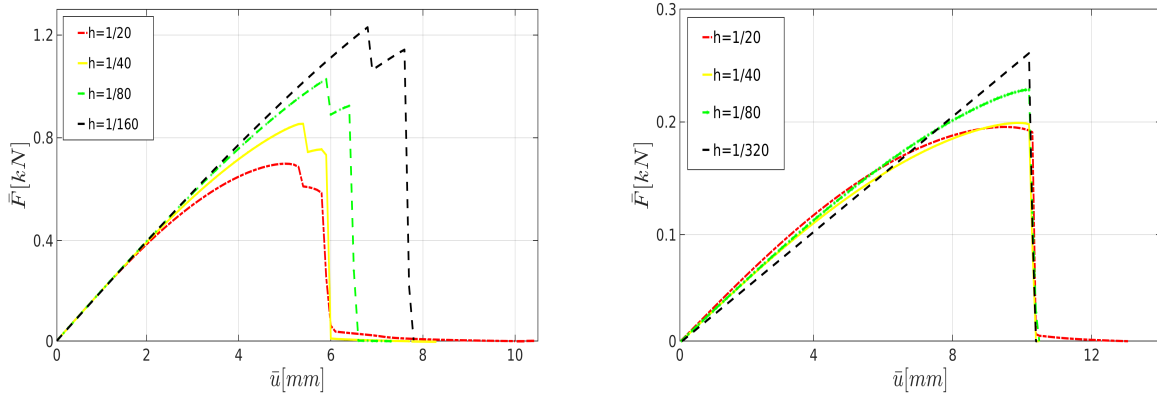


Figure 18: The displacement curve of DENT (Example 2) with different mesh sizes. Here the parameters are chosen according to the prior (left) and posterior (right) distributions.

Due to the resemblance to the first example (SENT) we use the same range of parameters. The load-displacement curves obtained from different values of μ , λ , and G_c are illustrated in Figure 20.

This numerical example includes two voids results in multi-stage crack propagation. Hence, in the load-displacement curve, two peak points exist to demonstrate multi-stage crack propagation, see Figure 20.

Figure 21 shows the proposal distribution where a uniform prior distribution is used for Bayesian inversion. Here

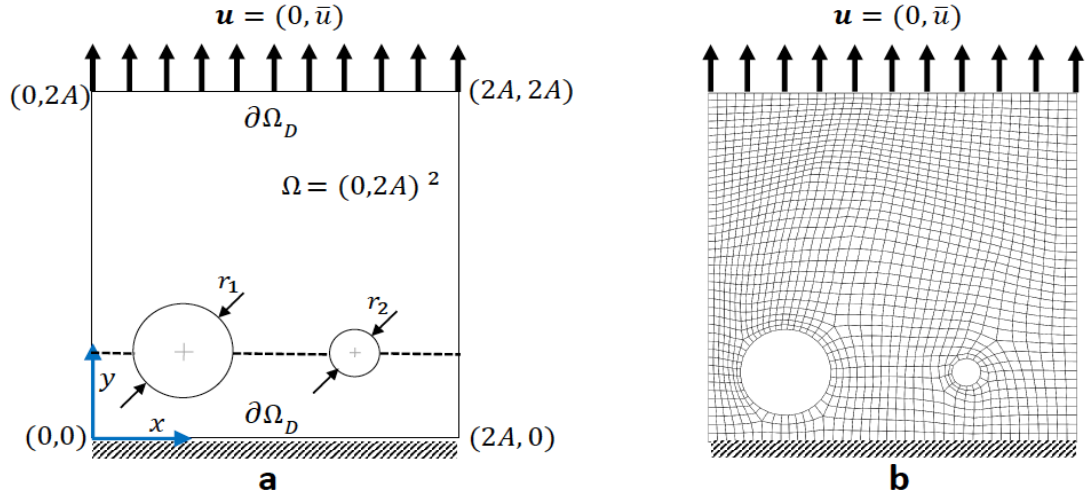


Figure 19: Schematic of SENT with voids (Example 3) (left) and its corresponding meshes with $h = 1/40$ (right).

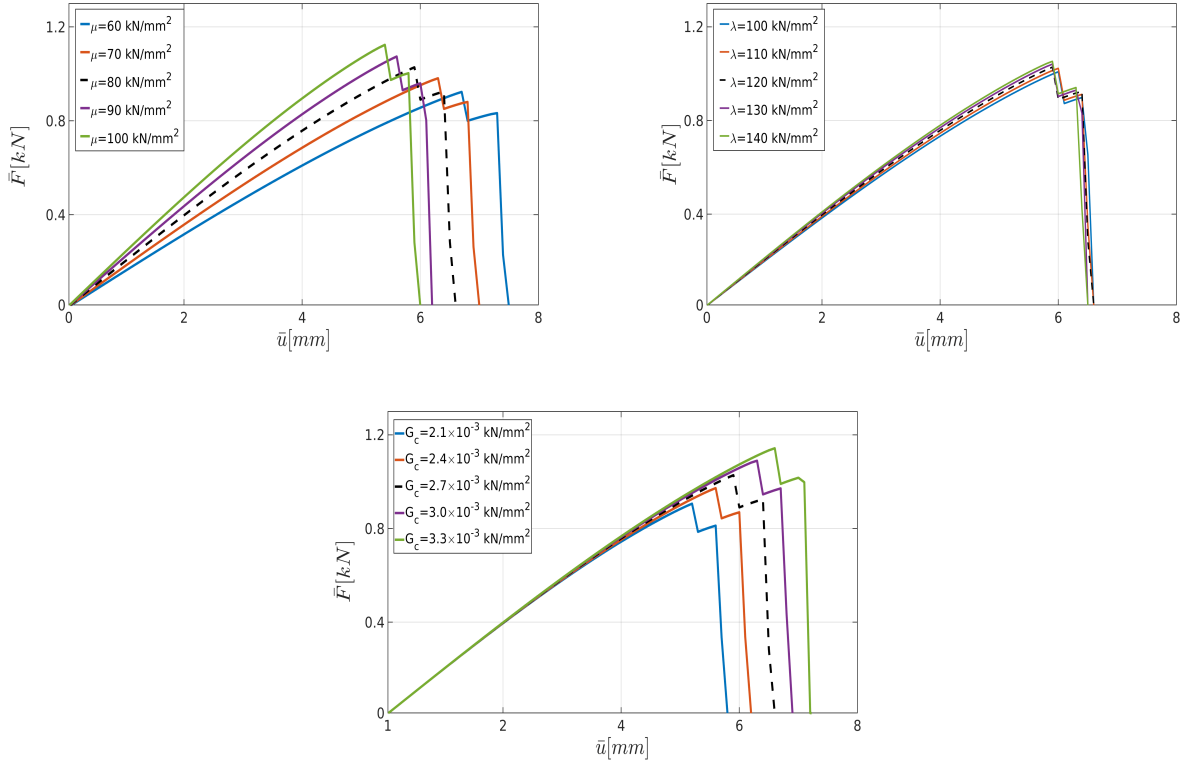


Figure 20: The force/displacement curve for different values of μ (top left), λ (top right) and G_c (bottom) for the SENT voids example (Example 3).

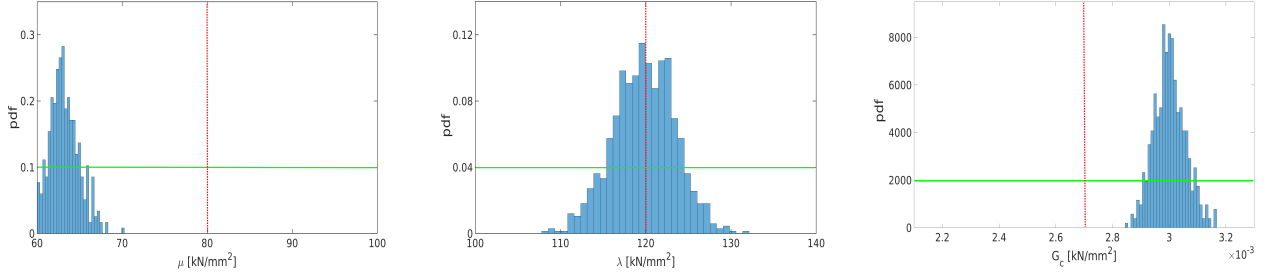


Figure 21: The prior (green curve), the mean value (red line), and posterior (histogram) distribution of μ (the first column), λ (the second column) and G_c (the third column) of SENT with voids (Example 3).

we use $h = 1/160$ as the reference solution and $h = 1/80$ is employed to estimate the parameters. As the diagrams show, most of the candidates for μ around the mean are rejected and only proposals less than 70 kN/mm^2 are accepted. Due to the smaller influence of λ , the accepted candidates are around the mean value (120 kN/mm^2) with a noticeably higher acceptance rate. In summary, the mean values are $\mu = 63 \text{ kN/mm}^2$, $\lambda = 120 \text{ kN/mm}^2$, and $G_c = 0.003 \text{ kN/mm}^2$, and the acceptance rates are 13%, 33%, and 19%, respectively.

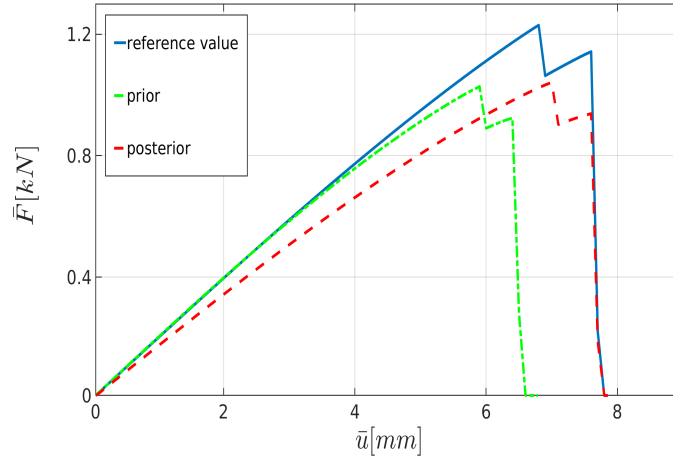


Figure 22: The load-displacement diagram of SENT with voids (Example 3). The parameters are the mean values ($\mu = 80 \text{ kN/mm}^2$, $\lambda = 120 \text{ kN/mm}^2$, and $G_c = 2.7 \times 10^{-3} \text{ kN/mm}^2$) obtained by one- and three-dimensional Bayesian inference.

We solve the forward model with the mean values of the estimated parameters. As Figure 22 shows, the difference between the prior distribution and the reference solution is significantly large. By using Bayesian inversion, we could compensate this difference; crack initiation and material failure points are estimated precisely. Although multidimensional Bayesian inversion increases the computational costs (CPU time), the estimated solution is closer to the reference value.

Finally, we show the crack patterns obtained by different meshes varying from $h = 1/10$ to $h = 1/160$. We

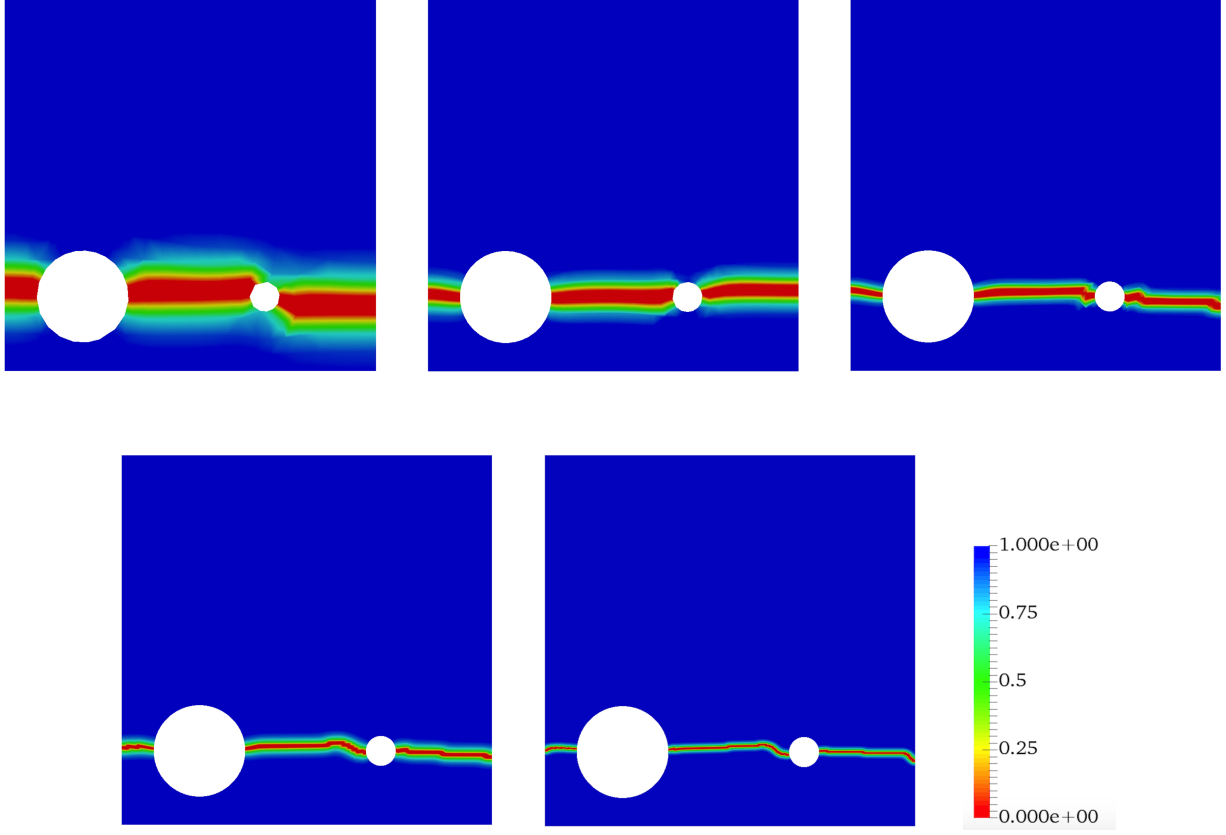


Figure 23: The effect of the mesh size on the crack propagation. The mesh sizes are (from the left) $h = 1/10$, $h = 1/20$, $h = 1/40$, $h = 1/80$, and $h = 1/160$ (the reference).

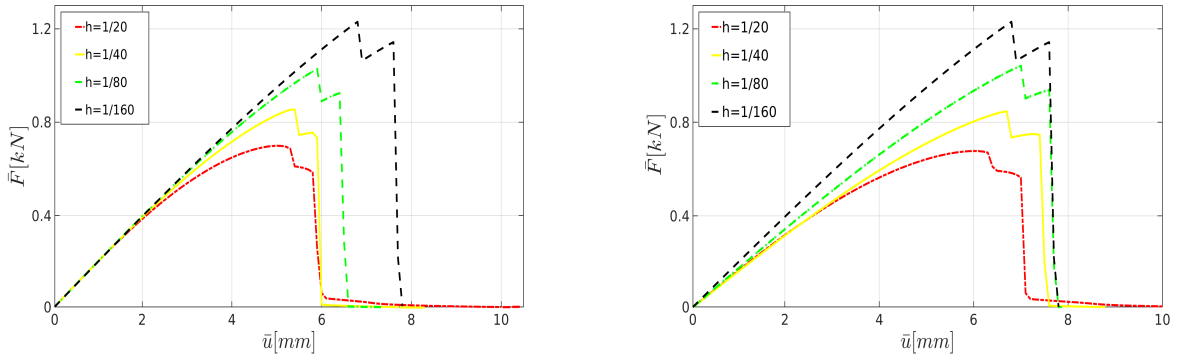


Figure 24: The displacement curve for different mesh sizes for SENT with voids. The effective parameters are chosen according to the prior (left) and posterior distributions.

use Bayesian inference to estimate the unknown parameters with the three-dimensional approach for $h = 1/20$ and $h = 1/40$. As Figure 24 illustrates, although the solution based on the posterior distribution is more precise (i.e., a

better estimation of crack initiation and the fracture point) compared to the one based on the prior distribution, there is still a difference compared to the reference value. These results conform to Figure 23, since the estimated crack pattern is considerably larger than the reality.

6. Conclusions and future works

In this work, we proposed a Bayesian approach to estimate the material parameters in a fracture process. For the fracture model, we adopted a phase-field approach, and for the parameter estimation, we employed a Bayesian framework. We studied three phase-field fracture settings, and in each one, Lamé's constants as well as the critical elastic energy release rate were estimated with respect to a reference solution.

The promising achievement in this work is significant reduction in computational time. By using Bayesian inversion, we could estimate the load-displacement curve precisely even with coarse meshes. For instance, in the first example (SENT), the diagram for $h = 1/320$ and $h = 1/80$ are essentially same, although a noticeable CPU time reduction is achieved. Interestingly, using even coarser meshes, the crack initiations and material fracture times can be estimated very well in all examples.

In future works, we will further reduce the computational cost by implementing local mesh adaptivity (see, e.g., [7]) or a global-local approach as an alternative in which the fine scale problem is dynamically chosen at each loading step [15]. The Bayesian approach will be used in multiscale problems to study crack propagation in heterogeneous materials, e.g., in composites. Due to their complexities, Bayesian inference will be employed to estimate material properties when the fiber reinforced structures have a random distribution.

7. Acknowledgments

T. Wick and N. Noii have been financially supported by the German Research Foundation, Priority Program 1748 (DFG SPP 1748) in the subproject *Structure Preserving Adaptive Enriched Galerkin Methods for Pressure-Driven 3D Fracture Phase-Field Models* with the project No. 392587580. A. Khodadadian and C. Heitzinger acknowledge financial support by FWF (Austrian Science Fund) START Project no. Y660 *PDE Models for Nanotechnology*. M. Parvizi has been supported by FWF *Project no. P28367-N35*.

References

- [1] G. Francfort, J.-J. Marigo, Revisiting brittle fracture as an energy minimization problem, *Journal of the Mechanics and Physics of Solids* 46 (8) (1998) 1319–1342.
- [2] B. Bourdin, G. Francfort, J.-J. Marigo, The variational approach to fracture, *Journal of Elasticity* 91 (2008) 5–148.
- [3] L. Ambrosio, V. Tortorelli, On the approximation of free discontinuity problems, *Bollettino dell'Unione Matematica Italiana* 6 (1992) 105–123.
- [4] A. Braides, *Approximation of free-discontinuity problems*, no. 1694, Springer Science & Business Media, 1998.

- [5] N. Noii, T. Wick, A phase-field description for pressurized and non-isothermal propagating fractures, *Computer Methods in Applied Mechanics and Engineering* 351 (2019) 860–890.
- [6] K. Mang, T. Wick, Numerical methods for variational phase-field fracture problems, *Lecture notes at Leibniz University Hannover* (2019).
- [7] T. Heister, M. F. Wheeler, T. Wick, A primal-dual active set method and predictor-corrector mesh adaptivity for computing fracture propagation using a phase-field approach, *Computer Methods in Applied Mechanics and Engineering* 290 (2015) 466–495.
- [8] T. Heister, T. Wick, Parallel solution, adaptivity, computational convergence, and open-source code of 2d and 3d pressurized phase-field fracture problems, *PAMM* 18 (1) (2018) e201800353.
URL <https://onlinelibrary.wiley.com/doi/abs/10.1002/pamm.201800353>
- [9] S. Burke, C. Ortner, E. Süli, An adaptive finite element approximation of a generalized Ambrosio-Tortorelli functional, *M3AS* 23 (9) (2013) 1663–1697.
- [10] S. Burke, C. Ortner, E. Süli, An adaptive finite element approximation of a variational model of brittle fracture, *SIAM J. Numer. Anal.* 48 (3) (2010) 980–1012.
- [11] M. Artina, M. Fornasier, S. Micheletti, S. Perotto, Anisotropic mesh adaptation for crack detection in brittle materials, *SIAM J. Sci. Comput.* 37 (4) (2015) B633–B659.
- [12] T. Wick, Goal functional evaluations for phase-field fracture using PU-based DWR mesh adaptivity, *Computational Mechanics* 57 (6) (2016) 1017–1035.
URL <http://dx.doi.org/10.1007/s00466-016-1275-1>
- [13] K. Mang, M. Walloth, T. Wick, W. Wollner, Mesh adaptivity for quasi-static phase-field fractures based on a residual-type a posteriori error estimator, *GAMM-Mitteilungen* 0 (0) e202000003.
URL <https://onlinelibrary.wiley.com/doi/abs/10.1002/gamm.202000003>
- [14] T. Gerasimov, N. Noii, O. Allix, L. De Lorenzis, A non-intrusive global/local approach applied to phase-field modeling of brittle fracture, *Advanced modeling and simulation in engineering sciences* 5 (1) (2018) 14.
- [15] N. Noii, F. Aldakheel, T. Wick, P. Wriggers, An adaptive global-local approach for phase-field modeling of anisotropic brittle fracture, *arXiv:1905.07519* (2019).
- [16] V. H. Hoang, C. Schwab, A. M. Stuart, Complexity analysis of accelerated MCMC methods for Bayesian inversion, *Inverse Problems* 29 (8) (2013) 085010.
- [17] W. K. Hastings, Monte Carlo sampling methods using Markov chains and their applications.
- [18] A. Khodadadian, B. Stadlbauer, C. Heitzinger, Bayesian inversion for nanowire field-effect sensors, *arXiv preprint arXiv:1904.09848*.
- [19] S. Mirsian, A. Khodadadian, M. Hedayati, A. Manzour-ol Ajdad, R. Kalantarinejad, C. Heitzinger, A new method for selective functionalization of silicon nanowire sensors and Bayesian inversion for its parameters, *Biosensors and Bioelectronics* 142 (2019) 111527.
- [20] S. Minson, M. Simons, J. Beck, Bayesian inversion for finite fault earthquake source models i—theory and algorithm, *Geophysical Journal International* 194 (3) (2013) 1701–1726.
- [21] M. Cardiff, P. Kitanidis, Bayesian inversion for facies detection: An extensible level set framework, *Water Resources Research* 45 (10).
- [22] N. Noii, I. Aghayan, Characterization of elastic-plastic coated material properties by indentation techniques using optimisation algorithms and finite element analysis, *International Journal of Mechanical Sciences* 152 (2019) 465–480.
- [23] C. Miehe, S. Mauthe, Phase field modeling of fracture in multi-physics problems. part iii. crack driving forces in hydro-poro-elasticity and hydraulic fracturing of fluid-saturated porous media, *Computer Methods in Applied Mechanics and Engineering* 304 (2016) 619–655.
- [24] Y. Heider, B. Markert, A phase-field modeling approach of hydraulic fracture in saturated porous media, *Mechanics Research Communications* 80 (2017) 38–46.
- [25] Y. Heider, S. Reiche, P. Siebert, B. Markert, Modeling of hydraulic fracturing using a porous-media phase-field approach with reference to experimental data, *Engineering Fracture Mechanics* 202 (2018) 116–134.
- [26] D. Kinderlehrer, G. Stampacchia, *An Introduction to Variational Inequalities and Their Applications*, *Classics in Applied Mathematics*, Society for Industrial and Applied Mathematics, 2000.

- [27] F. Aldakheel, S. Mauthe, C. Miehe, Towards phase field modeling of ductile fracture in gradient-extended elastic-plastic solids, *PAMM* 14 (1) (2014) 411–412.
- [28] C. Miehe, M. Hofacker, F. Welschinger, A phase field model for rate-independent crack propagation: Robust algorithmic implementation based on operator splits, *Comput. Meth. Appl. Mech. Engrg.* 199 (2010) 2765–2778.
- [29] F. Aldakheel, B. Hudobivnik, A. Hussein, P. Wriggers, Phase-field modeling of brittle fracture using an efficient virtual element scheme, *Computer Methods in Applied Mechanics and Engineering* 341 (2018) 443–466.
- [30] S. Teichtmeister, D. Kienle, F. Aldakheel, M.-A. Keip, Phase field modeling of fracture in anisotropic brittle solids, *International Journal of Non-Linear Mechanics* 97 (2017) 1–21.
- [31] R. G. Ghanem, P. D. Spanos, *Stochastic finite elements: a spectral approach*, Courier Corporation, 2003.
- [32] R. C. Smith, *Uncertainty quantification: theory, implementation, and applications*, Vol. 12, SIAM, 2013.
- [33] A. M. Stuart, Inverse problems: a Bayesian perspective, *Acta numerica* 19 (2010) 451–559.
- [34] A. F. Smith, G. O. Roberts, Bayesian computation via the Gibbs sampler and related Markov chain Monte Carlo methods, *Journal of the Royal Statistical Society: Series B (Methodological)* 55 (1) (1993) 3–23.
- [35] B. Stadlbauer, A. Cossettini, D. Pasterk, P. Scarbolo, L. Taghizadeh, C. Heitzinger, L. Selmi, et al., Bayesian estimation of physical and geometrical parameters for nanocapacitor array biosensors, *Journal of Computational Physics* 397 (2019) 108874.